

Table of Contents

1 Superconducting Transport	1
1.0 Basic Concepts	3
1.0.1 Microscopic Quasiparticles	3
1.0.2 Mesoscopic Quasiparticles	8
1.0.3 Aluminum as Material Platform	11
1.0.4 Microwave Drive and Electromagnetic Phase	13
1.1 Microscopic Description	15
1.1.1 Superconducting Gap	16
1.1.2 Density of States	16
1.1.3 Tunnel Current	18
1.1.4 Photon-Assisted Tunneling	23
1.2 Macroscopic Description	25
1.2.1 Josephson Effect	25
1.2.2 Shapiro Steps	27
1.2.3 RCSJ Model	29
1.3 Mesoscopic Description	36
1.3.1 Andreev Reflection	36
1.3.2 Andreev Bound States	39
1.3.3 Multiple Andreev Reflection	40
1.3.4 Photon-Assisted Multiple Andreev Reflection	43
1.4 Stochastic Description	46
1.4.1 P(E)-Theory	47
1.4.2 Dynamical Coulomb Blockade	49
1.4.3 Incoherent Two-Electron Tunneling	52
1.4.4 Superconducting Single-Electron Transistor	55
1.5 Experimental Realization	59
1.6 TODO	59
References	61

Superconducting Transport

Superconductivity was first observed by Heike Kamerlingh Onnes in 1911, when the electrical resistance of mercury vanished abruptly upon cooling below 4.2 K. Shortly thereafter, the Meissner–Ochsenfeld effect revealed that superconductors also expel magnetic fields, establishing the two defining macroscopic properties of this quantum state of matter, perfect conductivity and perfect diamagnetism. [1, 2]

At its core, superconductivity originates from an effective attraction between electrons near the Fermi surface. When an electron moves through the metal, it slightly distorts the ion lattice, creating a transient region of enhanced positive charge. A second electron can be attracted to this distortion, resulting in a very weak but cooperative pairing mechanism mediated by lattice vibrations (phonons). Despite the underlying Coulomb repulsion, this mechanism allows pairs of electrons with opposite momentum and spin to form Cooper-pairs. When many such pairs form simultaneously, they condense into a coherent macroscopic quantum state capable of carrying electrical current without resistance.

The remainder of this chapter develops a comprehensive theoretical framework for superconducting transport from four complementary viewpoints. These perspectives differ in the degrees of freedom they emphasize quasi-particles, phase dynamics, transparency channels, and environmental fluctuations. Together form a consistent and unified picture of the phenomena observed in experiment.

The first part introduces the microscopic Bardeen–Cooper–Schrieffer theory. It describes how electrons near the Fermi surface pair in the weak-coupling limit, how this pairing leads to an energy gap and a characteristic quasi-particle density of states, and how these quantities manifest in tunneling spectroscopy and photon-assisted transport.

The second part presents the macroscopic phase-based description of superconducting weak links. Since the order-parameter amplitude is nearly constant in the tunneling limit, the phase becomes the sole dynamical variable controlling coherent Cooper-pair transport. This leads directly to the Josephson relations, the microwave-induced Shapiro steps, and the classical phase dynamics described by the RCSJ model, which incorporates dissipation and capacitance and forms the basis for interpreting real I – V characteristics.

The third part provides the mesoscopic description, which connects microscopic quasi-particle physics with macroscopic phase coherence. Here, Andreev reflection and multiple Andreev reflections govern charge transport in highly

transparent contacts, and the resulting I - V characteristics encode the microscopic transmission properties of the junction.

Finally, the stochastic description accounts for phase fluctuations in dissipative electromagnetic environments through $P(E)$ -theory. This framework captures how the impedance of the surrounding circuitry affects phase coherence, energy exchange, and the overall I - V characteristics.

Before turning to the detailed microscopic, macroscopic, mesoscopic, and stochastic descriptions, Sec. 1.0 collects the basic concepts and global definitions used throughout this chapter. It introduces the quasiparticle description and Drude picture of normal-state transport, the mesoscopic transport regimes and their formulation in terms of transmission channels, the properties of aluminum as the central material platform, and the generic microwave drive model employed in all driven-transport scenarios.

1.0 Basic Concepts

In this section we collect the basic microscopic and mesoscopic concepts that underlie all transport phenomena discussed in this thesis. We start from a many-electron Hamiltonian in a crystalline solid and show how its low-energy excitations can be described in terms of quasiparticles with effective mass, lifetime, and mean free path, leading to the Drude picture of diffusive transport. On this basis we introduce the mesoscopic transport regimes, where the finite size of the conductor and phase coherence across it become essential and transport is most naturally formulated in terms of transmission channels and their eigenvalues. We then specialize to aluminum, which serves as the central material platform of this work, and summarize the normal-state, superconducting, and oxide properties that make it ideally suited for atomic-scale contacts and tunnel junctions. Finally, we outline the generic microwave drive model used throughout the thesis and the associated electromagnetic phase factors that give rise to photon-assisted tunneling and driven Josephson dynamics.

In this chapter we deliberately focus on a minimal set of effective parameters and working concepts; more detailed microscopic derivations and material-specific refinements are deferred to the specialized chapters where they become relevant. [3, 4]

1.0.1 Microscopic Quasiparticles

We consider a many-electron system in a crystalline solid and show how its low-energy excitations can be described in terms of quasiparticles. The full Hamiltonian (first quantization) for N electrons and fixed ionic cores at positions $\{\vec{r}_i\}$ is

$$\hat{H} = \sum_{i=1}^N \left(\frac{\hat{\vec{p}}_i^2}{2m} + V_{\text{ion}}(\vec{r}_i) \right) + \frac{1}{2} \sum_{i \neq j} \frac{e^2}{4\pi\varepsilon_0 |\vec{r}_i - \vec{r}_j|}, \quad (1)$$

with canonical momenta $\hat{\vec{p}}_i = -i\hbar\nabla_i$ and electron mass m . The ionic potential $V_{\text{ion}}(\vec{r})$ represents the Coulomb attraction of the electrons to the positively charged lattice. To a good approximation it is periodic,

$$V_{\text{ion}}(\vec{r} + \vec{R}) = V_{\text{ion}}(\vec{r}) \quad (2)$$

for all Bravais lattice vectors \vec{R} .

The many-electron wave function $\Psi(\vec{r}_1, \dots, \vec{r}_N, t)$ obeys the time-dependent Schrödinger equation

$$i\hbar \frac{\partial}{\partial t} \Psi = \hat{H} \Psi, \quad (3)$$

supplemented by antisymmetry under particle exchange due to Fermi statistics. Solving this problem exactly is not feasible. To arrive at a tractable description of electronic transport we now introduce a sequence of simplifications. [3, 4]

Effective One-Electron Description

First, according to the Born–Oppenheimer approximation, the fast electronic motion is separated from the slow ionic motion, and the ions are treated as fixed classical scatterers that generate the periodic potential $V_{\text{ion}}(\vec{r})$ plus some weak disorder. Next, electron–electron interactions are taken into account in an average way. Screening in a metal strongly reduces the long-range Coulomb repulsion, and the dominant effect of interactions can be encoded in an effective potential and a renormalized band structure. On this level, the complicated many-electron problem is reduced to an effective one-electron eigenvalue problem

$$\hat{H}_{\text{eff}} \psi(\vec{r}) = E \psi(\vec{r}), \quad \hat{H}_{\text{eff}} = \frac{\hat{\vec{p}}^2}{2m} + V_{\text{per}}(\vec{r}), \quad (4)$$

where $V_{\text{per}}(\vec{r})$ is a periodic effective potential that already includes the mean-field action of the other electrons. Residual interactions and disorder manifest at low energies through renormalized band parameters and relaxation processes that we summarize below by a small set of effective quasiparticle parameters.

The stationary eigenvalue problem with a periodic potential,

$$\left[-\frac{\hbar^2}{2m} \nabla^2 + V_{\text{per}}(\vec{r}) \right] \psi(\vec{r}) = E \psi(\vec{r}), \quad (5)$$

is the starting point for band theory. [5, 3, 6]

Bloch States and Band Structure

Because $V_{\text{per}}(\vec{r})$ has the periodicity of the lattice, Bloch's theorem applies. The eigenstates of \hat{H}_{eff} can be chosen as Bloch functions

$$\psi_{n\vec{k}}(\vec{r}) = e^{i\vec{k}\cdot\vec{r}} u_{n\vec{k}}(\vec{r}), \quad (6)$$

where n is a band index, \vec{k} lies in the first Brillouin zone, and $u_{n\vec{k}}(\vec{r} + \vec{R}) = u_{n\vec{k}}(\vec{r})$ is lattice-periodic. Inserting Eq. (6) into Eq. (5) yields for each \vec{k} a discrete set of eigenvalues $E_n(\vec{k})$ that define the band structure.

The Bloch functions form an orthonormal basis. In the independent-electron approximation, the many-electron ground state is obtained by filling the one-particle eigenstates up to the Fermi energy E_F , with at most two electrons (spin up and spin down) per state. For a given electron density, the filling of the bands fixes E_F and the corresponding Fermi surface defined by

$$E_n(\vec{k}) = E_F. \quad (7)$$

In simple metals one or a few bands cross the Fermi level. For transport at low temperature and low bias, only states in a narrow energy window $|E - E_F| \sim \max(k_B T, eV)$ are relevant. In this regime, the detailed band structure away

from the Fermi surface is irrelevant and can be compressed into a small set of effective parameters such as the Fermi velocity and the density of states at the Fermi energy. [3, 6]

Semiclassical Dynamics and Scattering

To connect this microscopic picture to transport, we consider how Bloch electrons move in weak external fields. On length and time scales large compared to the lattice spacing and inverse band gaps, the dynamics of an electron wave packet built from states in a single band n can be described semiclassically by

$$\hbar \frac{d\vec{k}}{dt} = -e \left(\vec{E} + \frac{d\vec{r}}{dt} \times \vec{B} \right), \quad \frac{d\vec{r}}{dt} = \frac{1}{\hbar} \nabla_{\vec{k}} E_n(\vec{k}), \quad (8)$$

where $d\vec{r}/dt$ is the group velocity, given by the gradient of the band energy, and \vec{E} , \vec{B} are external electric and magnetic fields. [3]

In a perfect, infinite crystal without interactions, Bloch electrons would evolve according to Eq. (8) and, for a uniform electric field, undergo Bloch oscillations rather than exhibit steady Ohmic transport. Real materials contain impurities, lattice defects, and phonons, and residual electron-electron interactions. These processes scatter carriers between Bloch states and thereby relax the current. [6, 7]

For the transport regimes relevant in this thesis it is sufficient to summarize all momentum-relaxing processes by a single (energy-averaged) momentum-relaxation time t_{qp} . The semiclassical picture then assumes that between scattering events electrons propagate as Bloch wave packets, while scattering events occur stochastically and randomize the momentum distribution. In the next subsection we recast this description in terms of quasiparticles and introduce the small set of effective parameters that will be used repeatedly. [3, 4]

Quasiparticles and Effective Single-Band Description

The independent-electron band picture treated interactions only at a mean-field level. In reality, the charged fermions in the Hamiltonian, which we will refer to as *electrons*, interact with each other and with lattice vibrations. The low-energy excitations of a metal are therefore not bare electrons but *quasiparticles*. In Landau's Fermi-liquid picture these quasiparticles are long-lived fermionic modes that carry charge $-e$ and spin $1/2$, but are dressed by their interaction with the surrounding Fermi sea. [8]

Throughout this thesis we characterize normal-state quasiparticles in a narrow energy window around E_F by a small set of effective parameters: an effective mass m^* , a Fermi velocity v_F , a (constant) normal-state density of states $N_0 = N(E_F)$, and a momentum-relaxation time t_{qp} . The corresponding elastic

mean free path is $\ell_{\text{qp}} = v_F t_{\text{qp}}$. Here, t_{qp} is a transport (momentum-relaxation) time and need not coincide with the single-particle lifetime that governs spectral broadening.

In an isotropic single-band approximation we approximate the dispersion by a parabolic form,

$$E(\vec{k}) \approx \frac{\hbar^2 |\vec{k}|^2}{2m^*}, \quad E_F = \frac{\hbar^2 k_F^2}{2m^*}. \quad (9)$$

The effective mass generally differs from the bare electron mass m and encodes both the band-structure curvature and renormalization due to interactions. The quasiparticle group velocity is then

$$\vec{v}(\vec{k}) = \frac{1}{\hbar} \nabla_{\vec{k}} E(\vec{k}) \approx \frac{\hbar \vec{k}}{m^*}, \quad (10)$$

and the Fermi velocity is $v_F = \hbar k_F / m^*$.

The density of states per unit volume for a three-dimensional parabolic band (with E measured from the band edge) reads

$$N(E) = \frac{1}{2\pi^2} \left(\frac{2m^*}{\hbar^2} \right)^{3/2} \sqrt{E}, \quad (11)$$

and evaluated at the Fermi energy yields $N_0 = N(E_F)$. Since E_F is of order eV whereas the relevant excitation energies are on the meV scale, $N(E)$ varies only weakly in the window of interest. It is therefore convenient to approximate it by a constant

$$N(E) \approx N_0 = N(E_F), \quad (12)$$

This approximation is accurate in the energy range relevant for low-temperature transport. Together with m^* and v_F , the momentum-relaxation time t_{qp} sets the characteristic transport scales (mean free path ℓ_{qp} and, in the diffusive limit, the diffusion constant), and provides the link between the microscopic quasiparticle picture and the macroscopic Drude description derived below. [3, 4]

Drude Model from the Microscopic Picture

Within the semiclassical picture the simplest transport model is the Drude description of a homogeneous metal. We treat the quasiparticles introduced above as classical point-like carriers with charge $-e$, effective mass m^* , and density n , which experience random momentum-relaxing collisions characterized by the relaxation time t_{qp} introduced above. In a weak, static electric field \vec{E} the equation of motion for the average quasiparticle momentum reads

$$\frac{d\langle \vec{p} \rangle}{dt} = -e\vec{E} - \frac{\langle \vec{p} \rangle}{t_{\text{qp}}}, \quad (13)$$

where the second term is a simple relaxation-time approximation for the effect of scattering. In the steady state, $d\langle \vec{p} \rangle / dt = 0$ and $\langle \vec{p} \rangle = -et_{\text{qp}} \vec{E}$. The average drift velocity is therefore

$$\vec{v}_{\text{drift}} = \frac{\langle \vec{p} \rangle}{m^*} = -\frac{et_{\text{qp}}}{m^*} \vec{E}. \quad (14)$$

Multiplying by the carrier density n gives the current density

$$\vec{j} = -nev_{\text{drift}} = \frac{ne^2 t_{\text{qp}}}{m^*} \vec{E}, \quad (15)$$

which identifies the Drude conductivity

$$\sigma = \frac{ne^2 t_{\text{qp}}}{m^*}. \quad (16)$$

In this bulk limit the system is assumed to be spatially homogeneous, and spatial variations of the electric field and current density are slow on the scale of the microscopic scattering lengths, such that transport is fully captured by the local constitutive relation $\vec{j} = \sigma \vec{E}$.

Integrating the local constitutive relation $\vec{j} = \sigma \vec{E}$ for a homogeneous wire of length L and cross-sectional area A yields the familiar macroscopic Ohm's law. In the conductance form that will be used throughout this thesis, one writes

$$I = G V, \quad G = \sigma \frac{A}{L}. \quad (17)$$

Equivalently, $V = IR$ with $R = 1/G$ and one may introduce the resistivity $\rho = 1/\sigma$ such that $R = \rho L/A$. While this bulk relation provides a convenient reference, it breaks down once the conductor becomes phase coherent and comparable in size to microscopic length scales, where transport must be described in terms of transmission channels as discussed below. [9]

Ohm's law provides a macroscopic relation between the measurable quantities I and V . The Drude picture goes one step further by linking this response to microscopic scattering. The same relaxation time t_{qp} that enters σ also sets the characteristic length and time scales of quasiparticle motion.

Momentum randomization over a time t_{qp} defines an elastic mean free path

$$\ell_{\text{qp}} = v_F t_{\text{qp}}, \quad (18)$$

where v_F is the Fermi velocity, and on longer scales the coarse-grained dynamics of the carrier density become diffusive with diffusion constant

$$D = \frac{v_F^2 t_{\text{qp}}}{3} = \frac{v_F \ell_{\text{qp}}}{3}. \quad (19)$$

These quantities σ , ℓ_{qp} , and D summarize the influence of microscopic scattering on transport in the bulk, diffusive limit and will serve as the reference point for the mesoscopic regimes discussed in the following subsection. [10]

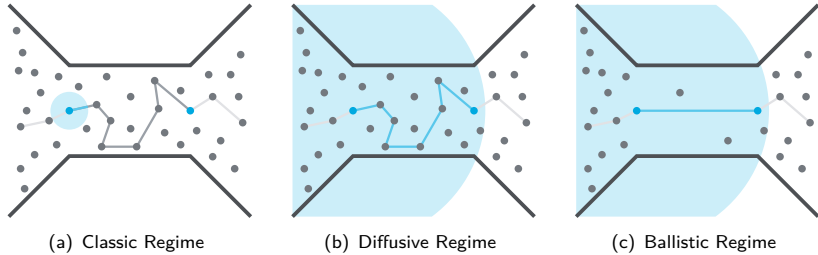


Figure 1 Schematic transport regimes set by the conductor length L , the elastic mean free path ℓ_{qp} , and the phase-coherence length ℓ_ϕ : (a) classical ($L \gg \ell_\phi, \ell_{qp}$), (b) phase-coherent diffusive ($\ell_{qp} \ll L \lesssim \ell_\phi$), and (c) ballistic ($L \ll \ell_{qp}, L \lesssim \ell_\phi$). The constriction (■) defines the scattering region of length L . Grey dots (■) indicate scattering centers, whose density sets ℓ_{qp} . A representative quasiparticle trajectory is shown, phase-coherent segments in blue (■) and phase-randomized segments in grey (■). The phase-coherence length is visualized by a disk of radius ℓ_ϕ (■).

1.0.2 Mesoscopic Quasiparticles

A key new ingredient of mesoscopic transport is the phase-coherence length ℓ_ϕ . It is set by inelastic and dephasing processes such as electron-electron and electron–phonon scattering and quantifies how far a quasiparticle can propagate while retaining a well-defined quantum phase. At finite temperature, quantum interference is additionally limited by thermal averaging, which is commonly characterized by the thermal length ℓ_T (defined below).

Mesoscopic transport refers to the regime in which the conductor size L becomes comparable to one or more microscopic length scales. The relevant hierarchy is set by the elastic mean free path ℓ_{qp} , which distinguishes ballistic from diffusive motion, and the phase-coherence length ℓ_ϕ , which distinguishes coherent from incoherent transport.

For macroscopic conductors, $L \gg \ell_{qp}$ and $L \gg \ell_\phi$, quasiparticles undergo many scattering events and lose phase coherence long before traversing the sample. Transport is then well described by the bulk Drude picture. In contrast, when $L \lesssim \ell_\phi$ phase coherence extends across the conductor and quantum interference between different scattering paths becomes observable. Whether this coherent regime is ballistic or diffusive is then decided by ℓ_{qp} . For $L \ll \ell_{qp}$ transport is ballistic and naturally described in terms of transmission channels. Whereas for $\ell_{qp} \ll L \lesssim \ell_\phi$ motion is diffusive but phase coherent and exhibits mesoscopic corrections to the Drude conductance. Figure 1 illustrates the relevant transport regimes. [3, 4]

Diffusive Mesoscopic Transport

In the diffusive mesoscopic regime the elastic mean free path remains much shorter than the system size, $\ell_{\text{qp}} \ll L$, so that quasiparticles undergo many momentum-randomizing scattering events while traversing the conductor. At the same time, phase coherence can persist over many such events, $L \lesssim \ell_\phi$, such that quantum interference between multiple scattering paths becomes observable.

For diffusive motion the phase-coherence length is conveniently expressed in terms of the diffusion constant D and a dephasing time t_ϕ ,

$$\ell_\phi = \sqrt{Dt_\phi}. \quad (20)$$

At finite temperature, interference is additionally reduced by thermal averaging over an energy window $\sim k_B T$. This introduces the thermal length

$$\ell_T = \sqrt{\hbar D/k_B T}, \quad (21)$$

such that phase-coherent effects are most pronounced when $L \lesssim \min(\ell_\phi, \ell_T)$.

On average, transport still follows the classical drift-diffusion picture with conductance and diffusion constant as introduced in the Drude model above. Quantum mechanically, however, the coherent superposition of scattering amplitudes produces characteristic corrections to the Drude conductance, most prominently weak localization and universal conductance fluctuations. In low-dimensional or strongly disordered systems these interference effects can become strong and may ultimately lead to Anderson localization. [11, 12, 13, 14, 15]

In the present work we only use the diffusive mesoscopic regime as a reference point for the ballistic limit realized in atomic-scale contacts.

Ballistic Transport and Transmission Channels

In the ballistic regime the length of the constriction is shorter than the elastic mean free path, $L \ll \ell_{\text{qp}}$, such that quasiparticles traverse the contact without momentum-randomizing scattering. If, in addition, the contact is shorter than the phase-coherence length, $L \lesssim \ell_\phi$, transport is phase coherent across the entire constriction. In the ballistic limit one may express the phase-coherence length in terms of the Fermi velocity and a dephasing time t_ϕ ,

$$\ell_\phi = v_F t_\phi. \quad (22)$$

In this regime resistance can no longer be attributed to dissipative processes distributed along the conductor. Instead, the constriction acts as an essentially elastic scatterer: partial reflection at the contact region limits the transmitted current, while the associated energy is ultimately dissipated in the reservoirs where quasiparticles relax.

A convenient description is provided by the scattering matrix of the contact. At a given energy E the leads support a finite number of transverse modes, and

the transmission properties are encoded in the transmission matrix $t(E)$. Its eigenvalues define transmission eigenchannels with probabilities

$$\{\tau_i(E)\} = \text{eig}(t^\dagger(E) t(E)) , \quad \tau_i(E) \in [0, 1] . \quad (23)$$

In the linear-response regime at low temperature the conductance of such a phase-coherent contact is given by the Landauer formula

$$G = G_0 \sum_{i=1}^N \tau_i , \quad G_0 = \frac{2e^2}{h} , \quad (24)$$

where $\tau_i \equiv \tau_i(E_F)$ are the transmission eigenvalues at the Fermi energy and G_0 is the conductance quantum¹. The full information about normal-state transport through the contact is thus encoded in the set of transmission eigenvalues $\{\tau_i\}$, often referred to as the mesoscopic *pin code* of the contact. [16, 17, 18]

Atomic-Scale Contacts

Metallic atomic contacts provide a paradigmatic realization of ballistic, phase-coherent transport. The constriction consists of only one or a few atoms, with a characteristic length of order an interatomic spacing. This scale is far shorter than the elastic mean free path and, at low temperature, also much shorter than the phase-coherence length, such that typically $L \ll \ell_{qp}$ and $L \ll \ell_\phi$.

In contrast to semiconductor quantum point contacts, where the number of channels is controlled by geometric confinement, the transmission eigenchannels of an atomic contact are set by the valence orbitals of the atoms forming the narrowest part of the constriction and by their hybridization with the electrodes. For aluminum, whose conduction states have predominantly *sp* character, this typically results in three dominant transport channels: one mainly *sp_z*-like channel and two transverse *p*-like channels. Depending on atomic geometry and disorder, additional weaker channels may appear, but the transport is usually governed by a small number of highly transparent modes.

Experimentally, the set of transmission probabilities $\{\tau_i\}$ can be extracted from superconducting transport measurements using multiple Andreev reflection and related techniques. Throughout this thesis we therefore characterize each atomic contact by its transmission eigenvalues (its mesoscopic *pin code*), which serve as input for the microscopic description of superconducting transport phenomena in the following chapters.

For comparison, quantum point contacts in high-mobility two-dimensional electron gases realize a similar ballistic, phase-coherent constriction, but with

¹Throughout this thesis the conductance quantum is defined as $G_0 \equiv 2e^2/h = 77.48 \mu\text{S}$. This value includes spin degeneracy and corresponds to the conductance of a fully transmitting normal-state channel. The corresponding resistance quantum is $R_0 = h/(2e^2) = 12.9 \text{ k}\Omega$.

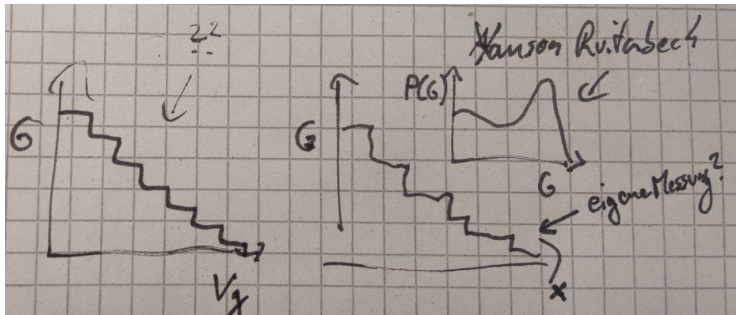


Figure 2 vgl. (a) qpc G over V_G , (b) opening trace aluminum G over Delta x , (c) histogram $P(G)$ over G of aluminum (Yanson ruitenbeck)

many channels whose number can be tuned electrostatically. There, the Landauer formula yields the well-known quantized conductance staircase $G \approx NG_0$ when each occupied mode is almost perfectly transmitted, $\tau_i \simeq 1$. While such semiconductor QPCs provide a clean didactic example of channel quantization, the focus of this work lies on metallic atomic contacts, where the number and transparency of channels are dictated by atomic-scale structure and chemistry rather than by lithographic geometry. [19, 20, 21]

1.0.3 Aluminum as Material Platform

Aluminum serves as the central material platform of this thesis. It provides both the normal-state metallic electrodes and the weak-coupling BCS superconductor in all transport experiments discussed in the following.

Aluminum is a simple sp metal with three valence electrons per atom and an fcc crystal structure. In the effective single-band picture introduced above, its low-energy normal-state properties can be summarized by the same quasiparticle parameters m^* , v_F , N_0 , and t_{qp} . Bulk aluminum is nearly free-electron-like, such that $m^* \simeq m$ is often a good approximation and the electronic energy scales are set by a large Fermi energy in the eV range. Correspondingly, the Fermi wavelength is on the sub-nanometer scale and the Fermi velocity is of order 10^6 m/s. In thin films, the elastic mean free path ℓ_{qp} can reach tens of nanometers in high-purity samples, but its precise value depends sensitively on disorder, thickness, and microstructure. [3, 4]

For mesoscopic aluminum structures the phase-coherence length ℓ_ϕ is not a fixed material constant but depends on temperature, disorder, and geometry. At sub-kelvin temperatures it is commonly of order micrometers, which justifies treating transport through atomic-scale contacts as fully phase coherent and ballistic, $L \ll \ell_{qp}, \ell_\phi$. At the atomic scale, the conduction channels in an aluminum

contact reflect the symmetry of the valence orbitals and their hybridization with the electrodes, typically resulting in one predominantly sp_z -like channel and two transverse p -like channels. These channel transparencies provide the central microscopic input for the superconducting transport models used throughout this thesis. [22]

Aluminum as Superconductor

As a superconductor, aluminum is a prototypical weak-coupling BCS material with an isotropic s -wave order parameter², and a well-understood phonon-mediated pairing mechanism.

The zero-temperature gap and critical temperature are, to good approximation,

$$\Delta_0 \approx 180 \text{ }\mu\text{eV}, \quad T_C \approx 1.2 \text{ K}. \quad (25)$$

The comparatively small gap places typical microwave frequencies well below the pair-breaking threshold³, enabling controlled photon-assisted processes without degrading superconductivity. [23, 24, 22]

The BCS coherence length in the clean limit is given by,

$$\xi_0 \simeq \hbar v_F / \pi \Delta_0, \quad (26)$$

yielding a value of order 1–2 μm for aluminum. In disordered (dirty) thin films, where $\ell_{qp} \ll \xi_0$, the effective coherence length is reduced and is well approximated by

$$\xi \simeq 0.85 \sqrt{\xi_0 \ell_{qp}} \simeq \sqrt{\frac{\hbar D}{2\pi k_B T_C}}. \quad (27)$$

For typical evaporated aluminum films with ℓ_{qp} in the range of a few tens of nanometers this gives ξ on the order of 100–300 nm. Together with its weak spin-orbit scattering and the availability of reproducible tunnel barriers (discussed below), these properties make aluminum ideally suited for tunneling spectroscopy and mesoscopic superconducting transport. [23, 24, 22]

Aluminum Oxide as Insulator

A key practical advantage of aluminum is its native oxide. Upon exposure to oxygen, aluminum rapidly forms a thin insulating AlO_x layer on its surface that

²Here and in the following, “ s -wave” refers to the isotropic angular dependence of the superconducting order parameter on the Fermi surface, classified by spherical harmonics, and should not be confused with atomic s orbitals. In aluminum the conduction band has predominantly sp -hybridized character, but the Cooper-pair wave function is s -wave in the sense of an isotropic pairing symmetry.

³The pair-breaking frequency of aluminum is given by $\nu_{pb} = 2\Delta_0/h \approx 87 \text{ GHz}$. For further information see Section 1.2.1.

passivates the metal and is strongly bound to the underlying film. Under ambient conditions this native oxide is typically only a few nanometers thick and self-limiting. By controlled oxidation in vacuum one can reproducibly tune the barrier properties and thereby the normal-state tunnel resistance over several orders of magnitude. The resulting Al–AlO_x–Al junctions are a standard workhorse of superconducting electronics and, when well fabricated, provide stable tunnel barriers with low subgap leakage.

In the context of this thesis, native and artificially grown aluminum oxide layers define the tunnel barriers in our SIS junctions and contribute to the mechanical stability of atomic contacts formed in aluminum break junctions. [24, 22, 25]

1.0.4 Microwave Drive and Electromagnetic Phase

Many of the transport phenomena discussed in this chapter involve the presence of a time-dependent electromagnetic drive. To avoid repeated introductions of the same setup, we summarize here the general assumptions that apply to all subsequent descriptions. The drive is treated as a classical, externally imposed field. No cavity modes or backaction of the junction onto the field are considered. The entire voltage drop is assumed to occur across the junction, a convenient gauge choice. In consequence, the electromagnetic field enters only through the scalar potential in the tunneling Hamiltonian or via the Josephson phase evolution. The drive amplitude is taken to be small enough not to heat the electrodes, allowing both to remain in local thermal equilibrium with Fermi–Dirac distributions. Finally, the drive frequencies are chosen such that photon energy is way smaller than the pair-breaking energy, ensuring that Cooper pairs remain intact while the phase dynamics are driven coherently. In practice, frequencies in the microwave range up to about 20 GHz are used. [26, 27, 28, 29]

The spatially uniform microwave field is then given by

$$V(t) = V_0 + A \cos(2\pi\nu t), \quad (28)$$

with a static component V_0 , drive amplitude A , and frequency ν .

Electromagnetic Phase

A time-dependent voltage does not only change the electrochemical potential of the electrodes but also imprints a time-dependent phase on any charged excitation that tunnels across the junction. In the gauge used here, the entire drive enters through the scalar potential $V(t)$ and appears as a phase factor multiplying the tunneling amplitude. The relevant quantity is the charge q carried by the process under consideration. For single-quasiparticle tunneling one has $q = e$, for Cooper-pair tunneling and single Andreev reflection processes $q = 2e$, and

for higher-order multiple Andreev reflections the effective transferred charge is an integer multiple $q = me$ with $m > 2$.

In general, the accumulated electromagnetic phase between time 0 and t is given by

$$\phi(t) = \frac{1}{\hbar} \int_0^t qV(t') dt', \quad (29)$$

and enters the tunneling matrix element as a phase factor.

Inserting the harmonic drive from Eq. (28), and performing the time integration separates the phase into a static and an oscillatory contribution,

$$\exp(-i\phi(t)) = \exp(-i\phi_0(t)) \exp(i\alpha \sin(2\pi\nu t)), \quad (30)$$

where

$$\phi_0(t) = \frac{qV_0 t}{\hbar} \quad \text{and} \quad \alpha = \frac{qA}{\hbar\nu} \quad (31)$$

denote the phase accumulated from the static bias and the dimensionless modulation strength, respectively. Both depend linearly on the transferred charge q and therefore distinguish quasiparticle, Cooper-pair, and higher-order Andreev processes within the same formalism.

The oscillatory phase factor is conveniently expanded using the Jacobi–Anger identity,

$$\exp(i\alpha \sin(2\pi\nu t)) = \sum_{n=-\infty}^{\infty} J_n(\alpha) \exp(in 2\pi\nu t), \quad (32)$$

where $J_n(\alpha)$ is the n -th Bessel function of the first kind. This harmonic decomposition will be used repeatedly in this chapter to describe photon-assisted tunneling processes for different effective charges $q = me$.

1.1 Microscopic Description

The microscopic description of superconductivity used here begins with the Bardeen–Cooper–Schrieffer (BCS) theory. In this framework, an effective phonon mediated attraction allows electrons near the Fermi surface to form bound pairs of opposite momentum and spin, so called Cooper pairs. The resulting condensate is characterized by a complex pairing order parameter whose magnitude determines the gap in the quasi-particle spectrum. In the microscopic tunneling regime considered here, only the quasi-particle spectrum and the magnitude of the gap enter. Phase coherence becomes relevant for transport only when the phase difference between two superconductors matters, as discussed in later sections. [30, 31]

A key assumption of the BCS framework is that this effective interaction is weak compared to the electronic energy scales of the metal. This situation is referred to as the weak-coupling limit. In this regime, the attractive interaction acts only within a narrow energy shell around the Fermi surface, typically a few meV compared to Fermi energies of several eV. As a result, only a small fraction of electrons near the Fermi level participate in pairing, while the rest of the electronic structure remains essentially unaffected. Because the coupling is weak, the resulting energy gap and the critical temperature are small but can be predicted with high accuracy from the microscopic parameters. For all numerical examples and illustrations in this chapter, aluminum is used as a representative weak-coupling BCS superconductor (Sec. 1.0.3).

The superconducting order parameter is the complex pairing amplitude

$$\Delta(\vec{r}) = |\Delta| \exp(i\phi(\vec{r})) . \quad (33)$$

Its magnitude represents the pairing strength and whose phase encodes macroscopic phase coherence. For the purposes of tunneling spectroscopy, only the magnitude $|\Delta|$ is experimentally relevant. In consequence, we treat Δ as a scalar quantity, i.e., we consider only its magnitude and assume a uniform, spatially constant phase, since tunneling spectroscopy in the weak-coupling limit is sensitive solely to the energy gap $|\Delta|$ and not to spatial or vectorial structure of the order parameter.

The following subsections introduce the key elements of this microscopic picture. First, the temperature dependence of the superconducting gap is discussed. Second, the superconducting DOS and introduce realistic broadening are derived. Third, these quantities are connected to tunneling spectroscopy through the microscopic expressions for the tunnel current. Finally, photon-assisted tunneling extends this static picture to driven transport in the presence of an oscillating electromagnetic field.

1.1.1 Superconducting Gap

In the weak-coupling limit, the theoretical treatment of superconductivity simplifies considerably. The normal-state density of states can be taken as constant in the narrow energy shell relevant for pairing, and the attractive interaction may be approximated as uniform across this shell. As a consequence, many observable quantities assume universal forms, most notably the ratio between the zero-temperature gap and the critical temperature,

$$\Delta_0 \approx 1.764 k_B T_C, \quad (34)$$

which holds for all weak-coupling BCS superconductors.

The superconducting gap, however, is not constant with temperature. At $T = 0$, electrons within the pairing shell around the Fermi energy form a condensate characterized by a well-defined order parameter. With increasing temperature, thermal excitations break an increasing fraction of Cooper pairs, reducing the number of electrons bound in the superconducting state. As fewer pairs contribute to the condensate, the magnitude of the order parameter decreases, and the energy required to break a pair, $\Delta(T)$, is gradually reduced.

This reduction proceeds smoothly until the critical temperature T_C is reached. At $T = T_C$, thermal fluctuations fully disrupt the pairing correlations, the order parameter vanishes continuously, and superconductivity is lost. The temperature dependence of the gap reflects the balance between the condensation energy gained by pairing and the entropy associated with thermal excitations. The universal weak-coupling curve is shown in Fig. 3.

In the BCS framework, the functional form of $\Delta(T)$ is obtained from the self-consistent gap equation. Its numerical solution yields a universal curve valid for all weak-coupling superconductors. A commonly used approximation to this solution is

$$\frac{\Delta(T)}{\Delta_0} \approx \tanh\left(1.74 \sqrt{\frac{T_C}{T} - 1}\right), \quad (35)$$

which reproduces the numerical result with high accuracy throughout the full temperature range. [32]

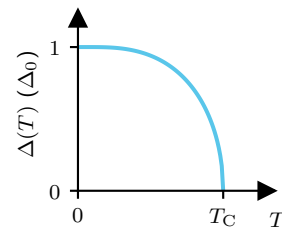


Figure 3 Temperature dependence of the superconducting gap $\Delta(T)$ in the weak-coupling limit.

1.1.2 Density of States

Throughout this section, energies are measured relative to the chemical potential, which for conventional metals coincides with the Fermi energy to very good

approximation. Thus $E = 0$ corresponds to the Fermi level around which superconducting correlations form.

In the normal state, the electronic density of states (DOS) varies only weakly with energy near the Fermi level. Over the narrow pairing shell relevant to weak-coupling superconductivity, this variation can be neglected and the DOS may be taken as constant. The corresponding value at the Fermi level is

$$N_0 \equiv \frac{1}{2\pi^2} \left(\frac{2m}{\hbar^2} \right)^{3/2} \sqrt{E_F}, \quad (36)$$

which follows from a free-electron parabolic dispersion and is an excellent approximation for aluminum.

When superconductivity sets in, pairing correlations reorganize this otherwise flat spectrum. A gap of width 2Δ opens around the Fermi level where single-particle excitations are absent in the ideal BCS limit. The spectral weight removed from the gap interior is redistributed to the gap edges, producing the characteristic coherence peaks. The resulting normalized DOS is

$$\frac{N_S(E)}{N_0} = \begin{cases} 0 & (|E| < \Delta) \\ \frac{|E|}{\sqrt{E^2 - \Delta^2}} & (|E| \geq \Delta) \end{cases}. \quad (37)$$

which diverges at the gap edges due to the flattening of the Bogoliubov quasi-particle dispersion. Within mean-field BCS theory this DOS is strictly sharp. Temperature affects only the occupation of the states through the Fermi–Dirac distribution and does not broaden the DOS itself.

Real superconductors, however, never exhibit perfectly sharp coherence peaks. A widely used and remarkably successful phenomenology is the Dynes broadening, which models finite quasi-particle lifetimes by the substitution $E \rightarrow E + i\gamma$

$$\frac{N_S(E)}{N_0} = \text{Re} \left(\frac{E + i\gamma}{\sqrt{(E + i\gamma)^2 - \Delta^2}} \right). \quad (38)$$

The Dynes parameter⁴ γ accounts for inelastic scattering, spatial inhomogeneity, pair breaking by magnetic impurities, or non-equilibrium effects, all of which smear the ideal BCS singularities. [33]

The DOS specifies the available single-particle states, whereas the Fermi–Dirac distribution determines their occupation at a given temperature. For conventional metals $\mu \approx E_F$, so the energy scale remains consistent with the above convention. The equilibrium occupation is

$$f(E) = \frac{1}{1 + \exp\left(\frac{E}{k_B T}\right)}, \quad (39)$$

⁴Throughout this work we distinguish between the Dynes broadening parameter γ , which enters the quasi-particle DOS in the microscopic tunneling description, and the tunneling rates Γ that appear in the stochastic description of incoherent charge transfer. These quantities refer to different physical mechanisms and should not be confused.

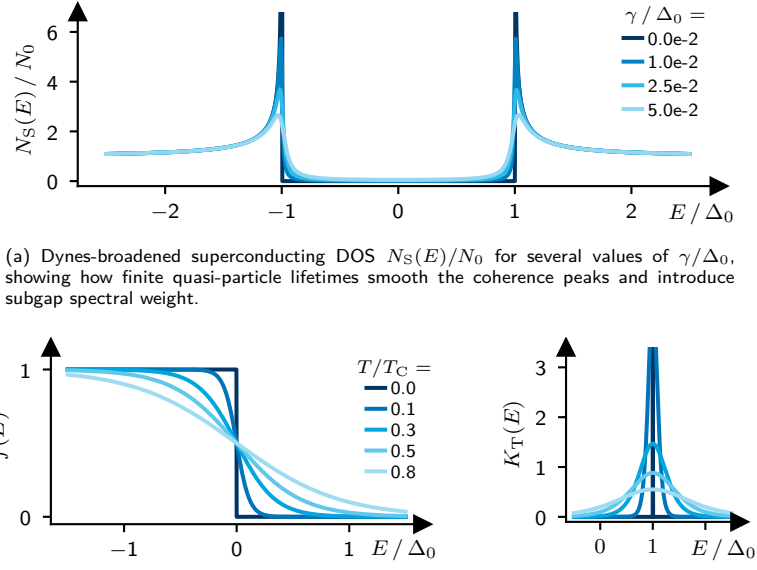


Figure 4 Together, these three ingredients determine the qualitative shape and resolution of the microscopic I - V and dI - dV characteristics. Parameters correspond to aluminum (Sec. 1.0.3).

which reduces to the step function $\theta(E)$ as $T \rightarrow 0$.

For future application, we can define the thermal broadening kernel

$$K_T(E) := -\frac{\partial f(E)}{\partial E}, \quad (40)$$

which reduces to a delta distribution $\delta(E)$ as $T \rightarrow 0$.

Figure 4(a) visualizes how Dynes broadening smooths the coherence peaks of $N_S(E)$, while Fig. 4(b) and (c) shows how finite temperature smears the Fermi edge and the thermal broadening kernel.

1.1.3 Tunnel Current

Tunneling spectroscopy provides a direct and conceptually transparent probe of the quasi-particle excitation spectrum. When two electrodes are separated by a sufficiently thin insulating barrier, electrons may tunnel quantum-mechanically between them even though the process is classically forbidden. In the tunneling limit, the barrier is high and wide enough that phase coherence between the

electrodes is lost and momentum conservation across the junction no longer applies. In this regime, tunneling reduces to an incoherent single-particle transfer process governed solely by the available electronic states and their occupation. [34, 35, 36]

Under these conditions, the microscopic current flowing from electrode 1 to electrode 2 is proportional to the number of occupied states at energy E in electrode 1 and the number of empty states at energy $E + eV$ in electrode 2

$$I_{1 \rightarrow 2}(V) \propto \int_{-\infty}^{\infty} (N_1(E)f_1(E)) \cdot (N_2(E + eV)(1 - f_2(E + eV))) dE, \quad (41)$$

where V is the externally applied bias voltage. The reverse process $2 \rightarrow 1$ is described by an analogous expression. Subtracting the two contributions yields the measurable tunnel current

$$I(V) = G_N \int_{-\infty}^{\infty} N_1(E) N_2(E + eV) (f_1(E) - f_2(E + eV)) dE, \quad (42)$$

where all geometric and matrix-element factors, as well as the constant DOS N_0 , are absorbed into the normal-state conductance G_N .

For some discussions, it's quite convenient to think about the tunnel current as a result of two convolutions⁵

$$I(V) = G_N [N_2(1 - f_2) \otimes N_1 - N_1 f_1 \otimes N_2](eV). \quad (43)$$

This equation highlights the two microscopic ingredients of tunneling. The densities of states $N_1(E)$ and $N_2(E)$, specifying where electrons may tunnel, and the Fermi–Dirac distributions, specifying which of those states are occupied. The factor $f_1(E) - f_2(E + eV)$ encodes the occupation imbalance created by the applied bias and ensures that current flows only when filled states in one electrode overlap with empty states in the other. The tunnel current therefore represents a convolution of the electronic structure of the two electrodes with their occupation functions, directly linking microscopic quasi-particle physics to the measurable I – V characteristics.

Throughout this section we adopt the asymmetric voltage convention, in which the applied bias shifts only the quasi-particle energies of electrode 2, $E \rightarrow E + eV$. This choice is equivalent to a gauge transformation and leaves the physics unchanged, but keeps the microscopic expressions particularly transparent.

Depending on whether either electrode is normal or superconducting, Eq. 42 reduces to three experimentally relevant cases.

⁵Convolution is mathematically defined as $(f \otimes g)(x) = \int f(y)g(x - y)dy$. A convolution weights all shifted copies of one function by another, expressing how strongly their features overlap as one is slid across the other.

N-N tunnel junction

In the case of a fully normal-conducting tunnel junction, both electrodes provide a flat density of states near the Fermi level. The microscopic expression for the current therefore reduces to

$$I_{NN}(V) = \frac{G_N}{e} \int_{-\infty}^{\infty} f(E) - f(E + eV) dE, \quad (44)$$

where all geometric and matrix-element factors, as well as the constant DOS N_0 , are absorbed into the normal-state conductance G_N . If both electrodes share the same temperature, the difference of Fermi functions integrates to the applied energy shift eV . The microscopic expression thus reproduces Ohm's law,

$$I_{NN}(V) = G_N V, \quad (45)$$

showing that an NN junction exhibits purely ohmic behaviour in the tunneling limit.

N-S tunnel junction

In a junction between a normal metal and a superconductor, the tunneling current becomes sensitive to the superconducting quasi-particle spectrum. Since the normal electrode provides a flat DOS, only the superconducting DOS enters the microscopic expression,

$$I_{NS}(V) = \frac{G_N}{e} \int_{-\infty}^{\infty} N_S(E) (f(E) - f(E + eV)) dE. \quad (46)$$

In the N-S case, one can probe the superconducting DOS, by measuring the dI/dV characteristic. It is proportional to the convolution, of the superconducting DOS with the thermal broadening kernel (Eq. 40). The thermal broadening kernel sets the fundamental energy resolution⁶ in N-S tunnel spectroscopy. However, it does not change the superconducting DOS, it alters the measured dI/dV . As temperature approaches zero, the dI/dV characteristic becomes directly proportional to the superconducting DOS.

Differentiating Equation 46 with respect to V acts only on the term $f(E + eV)$, since both $N_S(E)$ and $f(E)$ are independent of the applied bias. Using the chain rule, reveals the thermal broadening kernel at shifted energy $E + eV$. This

⁶A commonly used estimate is $\delta E \approx 3.5 k_B T$. At 30 mK (typical for a dilution refrigerator), this corresponds to about 10 μ eV, whereas at 300 mK (He_3 cryostat) the resolution is limited to about 100 μ eV. The relevant temperature is the electronic temperature, which can exceed the cryostat base temperature due to imperfect filtering, finite electron-phonon coupling, or microwave leakage.

results precisely in the convolution of the superconducting DOS with the thermal broadening kernel evaluated at the energy shift eV ,

$$\frac{dI_{NS}(V)}{dV} = G_N (N_S \otimes K_T)(eV). \quad (47)$$

These considerations directly underlie scanning tunneling microscopy, where a normal-metal tip above a superconducting surface realizes an N-S junction in the tunneling limit. Measuring the resulting I - V or dI - dV characteristics, at sufficiently low electronic temperatures, therefore provides a direct and spatially localized probe of the superconductor's quasi-particle DOS. In addition, the thermal broadening of the spectrum enables a reliable determination of the system's electronic temperature.

S-S tunnel junction

In a junction where both electrodes are superconducting, the tunnel current depends on the multiplicative overlap of the two gapped densities of states, evaluated at energies E and $E + eV$. The microscopic expression now reads

$$I_{SS}(V) = \frac{G_N}{e} \int_{-\infty}^{\infty} N_S(E) N_S(E + eV) (f(E) - f(E + eV)) dE. \quad (48)$$

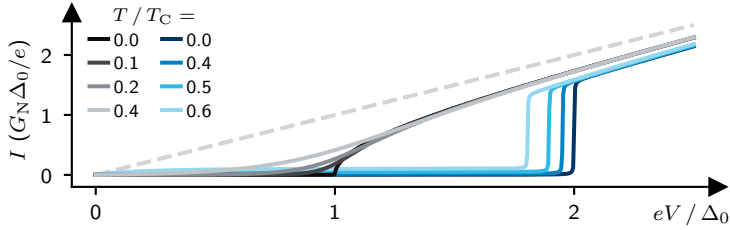
For S-S junctions, the differential conductance cannot be written as a convolution of the superconducting DOS with the thermal kernel. The shifted DOS $N_S(E + eV)$ carries an explicit voltage dependence, so differentiating the microscopic current generates additional contributions. Although the convolution form is sometimes quoted in the literature by analogy to the N-S case, this represents a misinterpretation and an unjustified generalization of the N-S result. However, there is a representation including the derivation of the DOS. At this point, an intuitive understanding for the differential conductance is not given anymore.

In contrast to the N-S case, the S-S differential conductance reflects the full multiplicative structure of the two gapped DOS. As a result, the onset of tunneling occurs only once $|eV|$ exceeds 2Δ , producing a pronounced threshold in both I - V and dI - dV .

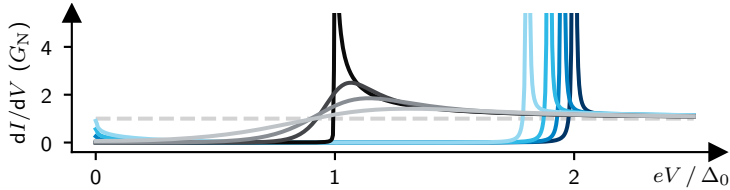
Figure 5 summarizes these effects and makes the contrasting roles of temperature and Dynes broadening in NS and SS junctions explicit.

In NS junctions, temperature primarily broadens the occupation factor and therefore rounds the coherence peak and smooths the gap edge, while Dynes broadening directly reduces the sharpness of the superconducting DOS itself.

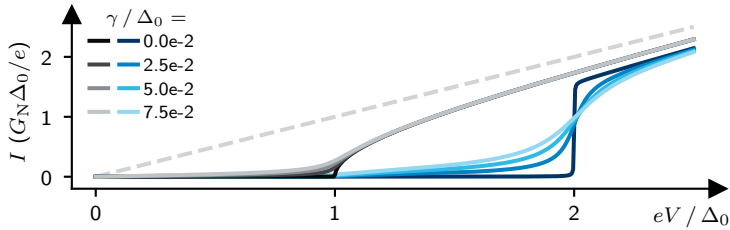
In SS junctions, the impact of both mechanisms is amplified by the multiplicative appearance of the DOS from each electrode. Temperature generates a noticeable subgap conductance and diminishes the peak height as it approaches the critical temperature. Whereas Dynes broadening suppresses the spectral features far more strongly than in the NS case due to its action on both electrodes simultaneously.



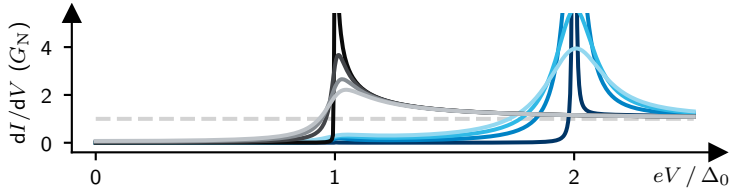
(a) Calculated I - V characteristics for different temperatures T/T_C at vanishing Dynes broadening ($\gamma = 0$). Increasing temperature rounds the coherence peaks and gradually fills the subgap region.



(b) Corresponding differential conductances dI/dV , showing the thermally induced suppression and broadening of the coherence peaks.



(c) Calculated I - V characteristics for different Dynes parameters γ/Δ_0 at $T = 0$. Lifetime broadening smooths the onset of quasi-particle tunneling and produces finite subgap conductance.



(d) Corresponding differential conductances dI/dV , illustrating the strong suppression and smearing of the coherence peaks due to lifetime broadening.

Figure 5 Temperature and Dynes broadening effects on NS (grey) and SS (blue) tunnel junctions within the microscopic tunneling model. Includes NN (light-grey dashed) junction for reference. Parameters correspond to aluminum (Sec. 1.0.3).

By fitting measured I - V or dI - dV data, with Δ_0 , T , and γ as variables, one can disentangle thermal effects from genuine lifetime or inelastic processes. These interpretations form the foundation of tunneling spectroscopy as a quantitative probe of superconductivity, allowing the extraction of these parameter from experimental data with high accuracy.

1.1.4 Photon-Assisted Tunneling

In the static tunneling expressions above, the Hamiltonian is time-independent and the Bardeen tunneling matrix element carries only its intrinsic phase. Once a microwave drive is applied, as introduced in Section 1.0.4, this matrix element acquires the time-dependent phase factor of Eq. 30. Here the relevant charge for quasi-particle tunneling is $q = e$. The drive thus modulates the single-electron tunneling phase, not the macroscopic superconducting phase, and this modulation is the microscopic origin of photon-assisted tunneling (PAT).

PAT remains an incoherent quasi-particle process. The AC drive mixes electronic energies separated by integer multiples of $\hbar\nu$, but it does not induce any phase-coherent Cooper-pair dynamics. This sharply distinguishes PAT from the Josephson phase dynamics responsible for Shapiro steps (Sec. 1.2.2).

The periodic phase modulation shifts the quasi-particle energy by discrete amounts. Let E_0 denote the unmodulated quasi-particle energy appearing in the static tunneling integral. Absorption or emission of $|n|$ photons then produces photon-shifted energies

$$E_n = E_0 + n\hbar\nu \quad (n \in \mathbb{Z}), \quad (49)$$

where $n > 0$ corresponds to absorption and $n < 0$ to emission. Using the Jacobi–Anger expansion of the global phase factor, the static quasi-particle DOS is replaced by the photon-dressed DOS

$$N(E_0) = \sum_{n=-\infty}^{\infty} J_n^2(\alpha) N(E_0 + n\hbar\nu), \quad (50)$$

where $\alpha = eA/\hbar\nu$ is the single-electron drive strength. Here, the photon-dressed DOS refers to the electrode whose quasi-particle energies are shifted by the applied bias, consistent with the asymmetric voltage convention used throughout this section.

Analogously, the tunnel current becomes a weighted sum of shifted copies of the static characteristic,

$$I(V_0) = \sum_{n=-\infty}^{\infty} J_n^2\left(\frac{eA}{\hbar\nu}\right) I_0\left(V_0 - \frac{n\hbar\nu}{e}\right), \quad (51)$$

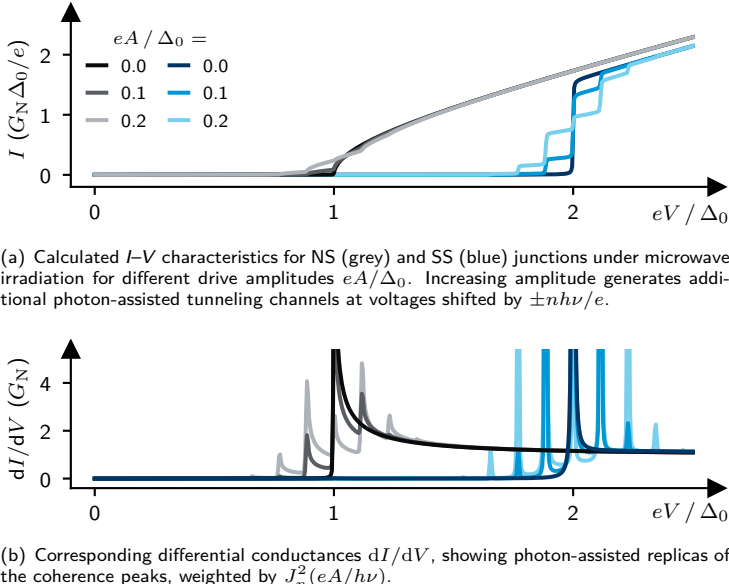


Figure 6 Photon-assisted tunneling in NS (grey) and SS (blue) junctions. The microwave drive couples electronic states differing in energy by $h\nu$, producing sideband replicas of the static I - V and dI - dV characteristics. Parameters correspond to aluminum (Sec. 1.0.3), with $T = 0$, $\gamma = 0$, and $\nu = 5.0$ GHz.

which is the Tien–Gordon result. Each term contributes a replica of $I_0(V_0)$ shifted by $nh\nu/e$ and weighted by the probability $J_n^2(\alpha)$ of absorbing or emitting $|n|$ photons. [28]

PAT therefore provides a universal semiclassical modification of quasi-particle tunneling. All differences between NS and SS junctions under microwave irradiation arise solely from their static DOS and not from the PAT mechanism itself. Figure 6 illustrates this behaviour for NS (grey) and SS (blue) junctions.

Experimentally, the drive amplitude A can be extracted from the relative sideband heights through the Bessel weights, while the spacing $h\nu$ between replicas provides a robust calibration of the microwave frequency. Photon-assisted tunneling thereby bridges static tunneling spectroscopy and driven superconducting transport in a fully microscopic and conceptually transparent way.

1.2 Macroscopic Description

While the previous section described dissipative transport in terms of single-particle tunneling, the complementary low-energy limit is governed by coherent Cooper-pair tunneling. In this regime, the quasiparticle spectrum plays no direct role. Instead, transport is determined solely by the phase of the superconducting gap introduced in Eq. 33. Because the magnitude $|\Delta|$ varies only weakly across a weak link, the relevant dynamical variable is the phase difference

$$\phi = \phi_1 - \phi_2, \quad (52)$$

which fully determines the supercurrent. The Josephson effect discussed here is treated in the weak-coupling (tunneling) limit, analogous to the quasiparticle tunneling regime introduced in the previous section. Figure 7 shows a schematic illustration of this situation.

A weak link, such as an insulating barrier, a metallic constriction, or a short normal region, allows the pairing potentials of the two superconductors to overlap. Since their amplitudes remain essentially constant on the junction scale, the coupling depends only on the relative phase. This phase difference is the essential quantity governing coherent Cooper-pair tunneling and forms the basis of the Josephson effect.

The following subsections introduce the two Josephson relations, discuss their physical implications, and develop the framework required to describe microwave-driven junctions and the RCSJ model.

1.2.1 Josephson Effect

When two superconductors are weakly coupled through a thin insulating barrier, constriction, or short metallic link, the amplitudes of their order parameters vary only minimally across the junction. The relevant degree of freedom is therefore the phase, which changes from ϕ_1 to ϕ_2 across the weak link. This phase difference ϕ governs the supercurrent flowing through the junction, and its maximum magnitude is set by the critical current I_C .

This perspective emphasizes that the Josephson effect arises from coherent phase coupling between the two superconductors, not from changes in the order-parameter amplitude. The resulting phase-driven transport is captured by two fundamental relations, known as the Josephson equations.

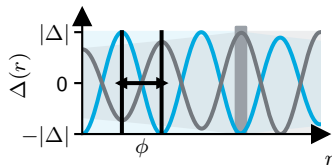


Figure 7 Spatial profile of $\Delta_1(r)$ (■) and $\Delta_2(r)$ (■) across a tunnel junction (■). Their respective magnitude $|\Delta|$ (shaded) varies only weakly across the barrier. Coherent coupling is governed by the macroscopic phase difference ϕ .

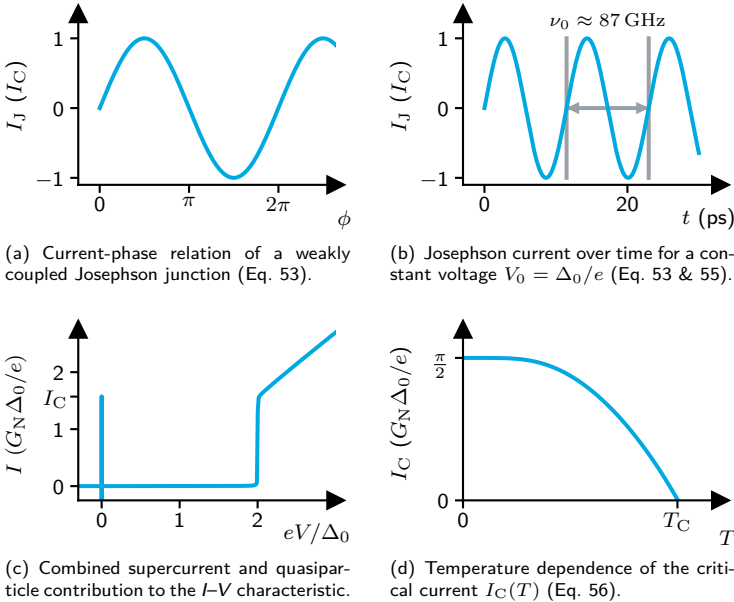


Figure 8 Josephson current over phase (a) and time (b). I - V characteristic (c) and temperature dependence of the critical current (d).

The DC Josephson effect is described by the current-phase relation (CPR)

$$I_J = I_C \sin \phi, \quad (53)$$

where I_C denotes the critical current of the weak link, as shown in Figure 8 (a). This CPR states that a dissipationless supercurrent can flow at zero voltage, driven solely by the phase difference between the two superconductors and is a direct consequence of coherent Cooper-pair tunneling.

The AC Josephson relation links the temporal evolution of the phase to the voltage across the junction,

$$\frac{d\phi}{dt} = \frac{2e}{\hbar} V_0, \quad (54)$$

implying that a constant voltage causes the phase difference to increase uniformly in time.

Consequently, the phase evolves linearly,

$$\phi(t) = \phi_0 + 2\pi\nu_0 t, \quad \nu_0 = \frac{2e}{\hbar} V_0, \quad (55)$$

which results in an oscillating supercurrent with frequency ν_0 . This is illustrated in Fig. 8 (b), where the time-dependent current $I(t)$ is shown together with the corresponding time scale $\Delta t = 1/\nu_0$ set by the Josephson frequency.

In a real junction, quasiparticle tunneling appears in parallel to the phase-driven supercurrent. The resulting I - V characteristic, shown in Fig. 8 (c), features a dissipationless supercurrent branch at zero voltage and a dissipative quasiparticle branch that onsets above the gap. This combined response forms the characteristic transport signature of a weakly coupled Josephson junction.

The critical current is set microscopically by the Ambegaokar–Baratoff (AB) relation,

$$I_C(T) = \frac{\pi}{2} \frac{G_N \Delta(T)}{e} \tanh\left(\frac{\Delta(T)}{2k_B T}\right), \quad (56)$$

shown in Fig. 8 (d). It reflects the BCS temperature dependence of the superconducting gap (Eq. 35) together with the thermal occupation of quasiparticle states. At zero temperature, the expression simplifies to the well known result $I_C = (\pi/2) G_N \Delta_0 / e$.

The strength of phase coupling in a Josephson junction is quantified by the Josephson energy

$$E_J = \frac{\hbar I_C}{2e}, \quad (57)$$

which sets the energetic stiffness of the phase and thus the robustness of coherent Cooper-pair tunneling. A large E_J corresponds to a well-defined phase, while a small E_J makes the junction susceptible to fluctuations.

Together with the thermal energy $E_T = k_B T$ and the charging energy $E_C = e^2/(2C)$, the Josephson energy sets the scale on which the phase behaves either classically or becomes susceptible to fluctuations. In the regime $E_J \gg \{E_T, E_C\}$, the phase is stiff and the Josephson relations hold in their ideal form, yielding a stable supercurrent. At finite temperature, thermally activated phase slips lead to a rounding of the sharp switching expected in an ideal I - V curve. This behavior is naturally described within the classical RCSJ framework, which incorporates thermal noise through the resistive branch. In the charge-dominated regime $E_C \gtrsim E_J$, quantum and fully stochastic descriptions of phase dynamics go beyond the classical RCSJ model and are discussed in Section 1.4.

Having established the phase dynamics in static conditions, we now turn to the interplay between the intrinsic Josephson oscillation and external microwave fields.

1.2.2 Shapiro Steps

When a Josephson junction is exposed to an external microwave field, the phase dynamics become modulated by the drive introduced in Section 1.0.4. The Josephson frequency ν_0 mixes with the external frequency ν , and the phase takes the form

$$\phi(t) = \phi_0 + 2\pi\nu_0 t + \alpha \sin(2\pi\nu t), \quad (58)$$

with $\alpha = 2eA/\hbar\nu$ the dimensionless drive strength.

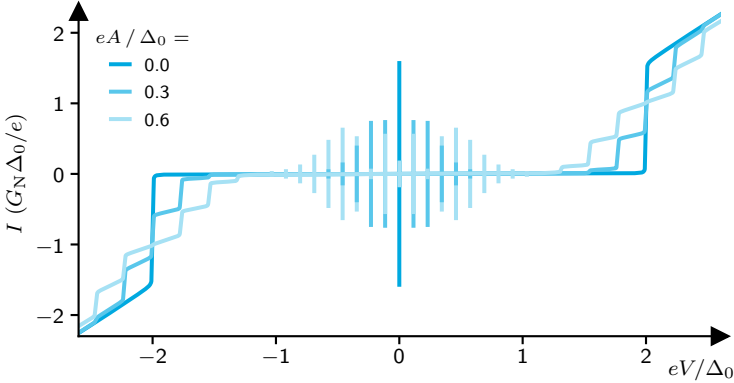


Figure 9 Microwave-driven transport in a weakly coupled Josephson junction. Parameters correspond to aluminum (Sec. 1.0.3), with $T = 0$, $\gamma = 0$, and $\nu = 10.0$ GHz.

Inserting this expression into the Josephson current-phase relation (Eq. 53) and expanding the phase modulation using the Jacobi-Anger identity (Eq. 32) yields harmonics at frequencies $\nu_0 - n\nu$. Whenever the resonance condition $\nu_0 = n\nu$ is satisfied, the n -th harmonic becomes stationary and contributes a finite dc component to the current. This produces quantized voltage plateaus at

$$V_n = \frac{n\hbar\nu}{2e}, \quad (59)$$

known as Shapiro steps.

The amplitude of each step is governed by the Bessel weight $J_n(\alpha)$, which reflects the strength of phase modulation by the microwave field. In contrast to the Tien–Gordon description of quasiparticle tunneling, the Bessel functions appear here without being squared because the Josephson current depends linearly on the phase modulation rather than on squared transition probabilities. Consequently, the step amplitudes scale as $J_n(\alpha)$ instead of $J_n^2(\alpha)$. The time-averaged I – V characteristic can therefore be written in direct analogy to the Tien–Gordon description,

$$I(V_0) = \sum_{n=-\infty}^{\infty} J_n(\alpha) I_0\left(V_0 - \frac{n\hbar\nu}{2e}\right), \quad (60)$$

where $I_0(V_0)$ denotes the static Josephson I – V curve in the absence of microwaves.

In a real junction, quasiparticle tunneling occurs in parallel with the phase-driven supercurrent. Under microwave irradiation, both Shapiro steps and PAT appear simultaneously. This combined response constitutes the characteristic microwave-driven transport signature of a weakly coupled Josephson junction.

As illustrated in Fig. 9, the interplay of phase locking and photon-assisted tunneling produces a rich structure in both the I - V and differential conductance characteristics.

1.2.3 RCSJ Model

The ideal Josephson relations describe how the supercurrent depends on the phase and how the phase evolves under a constant voltage. However, real junctions exhibit dissipation, capacitance, thermal fluctuations, and microwave-driven phase dynamics that cannot be captured by the ideal equations alone.

A convenient way to incorporate these additional contributions is to represent the junction as an effective circuit. To describe these effects, the Josephson element must be embedded into an effective circuit model.

Throughout this section, the junction is assumed to operate in the tunneling limit and in the classical regime $E_J \gg E_C, E_T$, such that phase dynamics are well described by the RCSJ equation without quantum corrections.

The resistively and capacitively shunted junction (RCSJ) model provides the minimal dynamical description of a real Josephson junction. It augments the ideal Josephson element by a normal resistance representing quasiparticle tunneling and a capacitance associated with the junction electrodes, as sketched in Fig. 10. These additions capture the essential dissipative and inertial mechanisms that govern the phase dynamics.

The damping regime encoded in the quality factor Q strongly affects the visibility and stability of microwave-driven features such as Shapiro steps.

Overdamped junctions exhibit clean, well-defined plateaus, whereas underdamped junctions show hysteresis and residual phase oscillations that distort the step structure.

In the following, we derive the RCSJ equation of motion for the phase and introduce the dynamical regimes that arise from the interplay of Josephson nonlinearity, dissipation, and inertia.

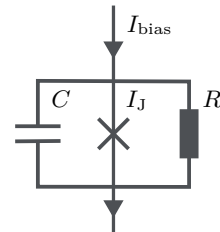


Figure 10 RCSJ model of a real Josephson junction.

Current Bias

To obtain the phase dynamics of the junction, the currents through the three parallel elements are summed according to Kirchhoff's law,

$$I_{\text{bias}} = I_C \sin(\phi) + \frac{V}{R} + C \frac{dV}{dt}. \quad (61)$$

We use I_{bias} to denote the externally applied current, distinguishing it from the Josephson supercurrent I_J , the resistive current, and the capacitive displacement current that appear in parallel in the RCSJ model.

Using the AC Josephson voltage-phase relation, this expression can be written entirely in terms of the phase,

$$I_{\text{bias}} = I_C \sin(\phi) + \frac{\hbar}{2eR} \frac{d\phi}{dt} + \frac{\hbar C}{2e} \frac{d^2\phi}{dt^2}. \quad (62)$$

This is the RCSJ equation of motion and forms the basis for all classical descriptions of Josephson phase dynamics. It contains an inertial term, a damping term, and the nonlinear Josephson restoring force, producing the characteristic tilted-washboard potential and the associated dynamical regimes discussed below.

Dimensionless RCSJ Model

To analyze the dynamics implied by Eq. 62, it is useful to cast the equation into a dimensionless form. This separates the contributions of inertia, damping, and the nonlinear Josephson term.

The natural time scale of the junction is set by the Josephson plasma frequency,

$$\omega_p = \sqrt{\frac{2eI_C}{\hbar C}}, \quad (63)$$

which determines the small-oscillation frequency of the phase in a potential minimum. It is distinct from the AC Josephson frequency, which reflects voltage-driven phase evolution, and instead characterizes the intrinsic resonance of the phase in the absence of bias.

Introducing the rescaled time $t' = \omega_p t$ and the normalized current $i = I_{\text{bias}}/I_C$ gives the compact dimensionless form

$$i = \sin \phi + \frac{1}{Q} \frac{d\phi}{dt'} + \frac{d^2\phi}{dt'^2}, \quad (64)$$

where the quality factor

$$Q = \sqrt{\frac{2eI_C R^2 C}{\hbar}} \quad (65)$$

quantifies the damping of the phase dynamics.

In this normalized form, the physical regimes become transparent. The second derivative describes inertial motion, $(1/Q)d\phi/dt'$ represents viscous damping due to the shunt resistor, and $\sin \phi$ provides the nonlinear restoring force from the Josephson coupling. The single parameter Q therefore distinguishes under-damped ($Q \gg 1$) from over-damped ($Q \ll 1$) junctions and sets the stage for the dynamical behavior discussed next.

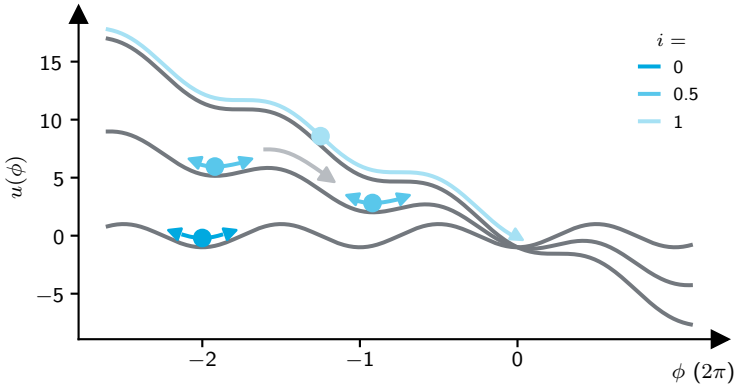


Figure 11 Tilted washboard potential of the RCSJ model (Eq. 67) for increasing normalized bias current i . For $i = 0$ (■) the phase is trapped in a stable minimum. At intermediate tilt, $0 < i < 1$ (□), the reduced barrier enables thermally activated or noise-driven phase slips (▨) between adjacent minima. At $i = 1$ (●) the barriers vanish and the phase runs downhill, corresponding to the finite-voltage state.

Tilted Washboard Potential

The normalized RCSJ equation 64, admits a mechanical interpretation that provides an intuitive picture of the phase dynamics. The equation is mathematically equivalent to the motion of a particle of unit mass in a tilted, periodic potential subject to viscous damping.

The normalized potential is obtained by identifying the restoring force with

$$-\partial u / \partial \phi = \sin \phi - i, \quad u = U/E_J, \quad (66)$$

which yields

$$u(\phi) = -\cos \phi - i \phi. \quad (67)$$

In the untilted case ($i = 0$) the barrier height is given by $\Delta U = 2E_J$. This "tilted washboard potential" consists of a cosine landscape whose overall slope is controlled by the normalized bias current i , as shown in Figure 11.

For small bias, $i < 1$, the potential exhibits a series of metastable minima. In this regime, the phase can remain localized in one of these wells, corresponding to the zero-voltage superconducting branch of the I - V characteristic. Small oscillations of the phase around the minimum occur at the plasma frequency defined in Eq. 63, but the average voltage remains zero.

As the bias is increased, the tilt of the potential grows and the barriers separating adjacent minima are reduced. At $i = 1$, the barriers vanish and the phase becomes free to run down the potential without encountering any local minima. This running solution corresponds to the finite-voltage, resistive state of

the junction. In the intermediate regime, fluctuations, either thermal or current-induced, can cause the phase to escape from a metastable minimum even for $i < 1$, giving rise to switching from the superconducting to the resistive branch.

A finite phase momentum acquired during escape might, once the bias is reduced again, retrap the phase only at a smaller tilt, leading to a retrapping back to the superconducting branch.

The washboard picture thus provides a unified interpretation of phase localization, escape, and running dynamics. It naturally explains the origin of the switching current, the emergence of retrapping current, and the role of thermal activation and noise, which are explored in the following subsections.

Switching Dynamics and Phase Diffusion

The switching current I_{SW} is the experimentally observed current at which a Josephson junction leaves the zero-voltage state and enters the resistive, running-phase regime. Unlike the intrinsic critical current I_C , which is a microscopic parameter set by the Josephson coupling energy, the switching current is a stochastic quantity. Its value is determined by the competition between the decreasing barrier height of the tilted washboard potential and fluctuations that drive premature escape. Thermal activation, current noise from the electromagnetic environment, and the rate at which the bias current is ramped all increase the likelihood of early escape and thus reduce the switching current below the critical current. Only in the ideal, noise-free limit does the switching current approach the intrinsic critical current.

In real Josephson junctions the supercurrent branch acquires a finite slope due to thermal and noise-induced fluctuations of the phase. Even for currents below the intrinsic critical value, stochastic forces drive small excursions of the phase within the tilted washboard potential, leading to a finite average phase velocity and hence a small, non-zero voltage. In the RCSJ model this effect is enhanced by the resistive branch in parallel with the Josephson element, which provides a dissipative path whenever the phase is not perfectly static. As a result, the ideal vertical supercurrent step is replaced by a broadened zero-voltage region whose slope grows with temperature, current noise and environmental damping.

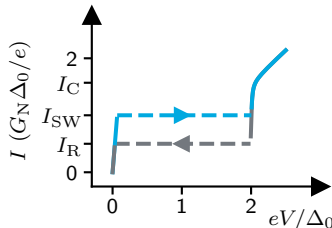


Figure 12 I - V characteristic of a Josephson junction in the intermediate damping regime ($Q \sim 1$), illustrating the combined effects of phase diffusion and residual inertia. Thermal and current noise produce a finite slope in the zero-voltage branch, while moderate damping leads to a hysteretic transition into the running state.

Retrapping Dynamics

After the phase has escaped into the running state, the junction develops a finite average voltage and the phase accelerates down the tilted washboard potential. When the bias current is reduced again, the junction does not immediately return to the zero-voltage state. Instead, the phase continues to move until sufficient kinetic energy has been dissipated for it to fall back into a metastable minimum. The current at which this return to the superconducting branch occurs is the retrapping current I_R .

In contrast to the switching current, set by escape from a minimum, the retrapping current reflects how efficiently damping removes the kinetic energy accumulated during the running state. Thermal and current noise smooth this transition, producing a broadened return to the superconducting branch rather than a sharp jump.

A representative I - V trace for this intermediate damping regime is shown in Fig. 12. It highlights the finite slope of the supercurrent branch due to phase diffusion, the broadened switching transition, and the smooth return at I_R characteristic of junctions with $Q \sim 1$.

In the overdamped limit ($Q \ll 1$), the phase has essentially no inertia. As soon as the bias is lowered below the point where the washboard potential recreates minima, the phase immediately relocks. The retrapping current equals the switching current.

In the underdamped limit ($Q \gg 1$), the phase retains significant kinetic energy after escape and cannot relock until the tilt is nearly removed. The retrapping current therefore approaches zero, giving rise to strong hysteresis in the I - V characteristic.

Shapiro Steps in the RCSJ Model

In the full RCSJ model, Shapiro steps arise through frequency locking between the intrinsic Josephson oscillation and an external microwave drive, as described in Section 1.0.4. The normalized RCSJ equation becomes

$$i + a \sin(2\pi\nu't') = \sin\phi + \frac{1}{Q} \frac{d\phi}{dt'} + \frac{d^2\phi}{dt'^2}, \quad (68)$$

where i is the normalized bias current. The normalized amplitude a and frequency ν are given by

$$a = A/I_C \sqrt{R^{-2} + (2\pi\nu C)^2}, \quad \nu' = \nu/\nu_p. \quad (69)$$

The washboard potential then becomes time dependent

$$u(\phi) = -\cos\phi - i\phi - a\phi \sin(2\pi\nu't'). \quad (70)$$

Weak damping makes the junction sensitive to residual oscillations, which can distort Shapiro steps and reduce their visibility under microwave irradiation.

In the overdamped regime, damping suppresses inertial phase oscillations and stabilizes the frequency-locked state, yielding clean, well-defined Shapiro steps. Thermal fluctuations broaden the step edges but do not compromise their visibility. This regime most closely reflects the behavior of the atomic aluminum contact studied in this work.

Figure 13 shows the resulting I - V characteristics in the under- and overdamped limit. The phase locks robustly to the external drive, producing a sequence of Shapiro plateaus.

The RCSJ framework bridges the gap between the ideal Josephson prediction of perfectly sharp Shapiro plateaus and the experimentally observed I - V characteristics, where damping, noise, and capacitive dynamics shape the visibility and stability of the steps.

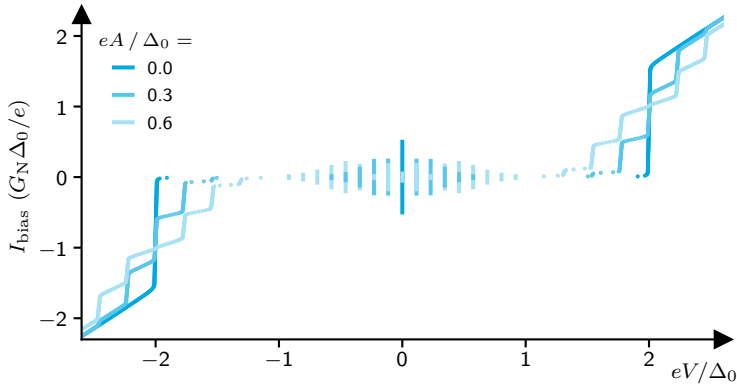
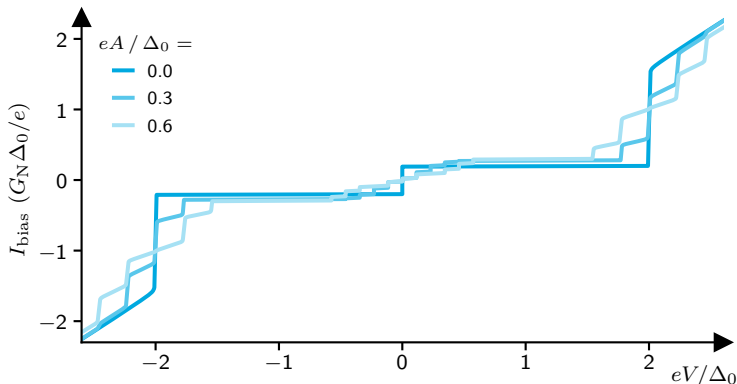
(a) Overdamped junction ($Q \ll 1$), switching current parameter $I_{\text{SW}} = 0.5 I_C$.(b) Underdamped junction ($Q \gg 1$), switching current parameter $I_{\text{SW}} = 0.2 I_C$.

Figure 13 Microwave-driven dc transport of a Josephson junction within the RCSJ model for (a) overdamped and (b) underdamped phase dynamics. Shown is the normalized bias current $I_{\text{bias}}/(G_N \Delta_0/e)$ versus the normalized voltage eV/Δ_0 for drive amplitudes $eA/\Delta_0 \in \{0, 0.3, 0.6\}$ at $\nu = 10$ GHz. Parameters correspond to aluminum (Sec. 1.0.3) with $T = 0$ and $\gamma = 0$.

1.3 Mesoscopic Description

In the mesoscopic regime, the electrodes are connected by a small number of quantum channels whose transmission probabilities τ_i determine the transport properties. This picture departs from both the microscopic description of quasi-particle tunneling and the macroscopic Josephson dynamics of weakly coupled junctions. Conduction is no longer a bulk property, but is governed by the discrete transmission eigenvalues of the available channels.

The natural starting point is the Landauer approach, originally formulated for phase coherent normal conductors. Each channel is characterized by a transmission probability τ_i , and the normal-state conductance reads

$$G_N = G_0 \sum_{i=1}^N \tau_i, \quad \tau_i \in [0, 1], \quad (71)$$

where G_0 is the conductance quantum accounting for spin degeneracy⁷.

Although the Landauer formula applies strictly to the normal state, the transmission eigenvalues remain well defined in superconducting contacts. For short, coherent junctions, the τ_i are set by the underlying scattering matrix and are essentially temperature independent.

These same transmission probabilities govern the amplitude of Andreev reflection, the energies of Andreev bound states, and the entire hierarchy of multiple Andreev reflection processes. The Landauer picture therefore provides the microscopic foundation of mesoscopic superconducting transport.

1.3.1 Andreev Reflection

At a normal-superconductor (N-S) interface, quasi-particles with energies $|E| < \Delta$ cannot enter the superconductor as single electrons because no states exist within the superconducting gap. Instead, an incident electron is retro reflected as a hole, while a Cooper pair carrying charge $2e$ is added to the condensate. This process, known as Andreev reflection (AR), preserves both charge and parallel momentum at the interface and provides the fundamental link between normal-state transport and superconducting correlations.

Andreev reflection can equivalently be viewed as the coherent transfer of two electrons into the superconductor, where they combine to form a Cooper pair. The probability of AR depends on the interface transparency. It reaches unity for a perfectly transparent contact and decreases when a potential barrier introduces normal reflection. The Andreev approximation applies when the Fermi energies of

⁷Throughout this thesis the conductance quantum is defined as $G_0 = 2e^2/h = 77.48\,\mu\text{S}$. This value includes spin degeneracy and corresponds to the conductance of a fully transmitting normal-state channel. The corresponding resistance quantum is $R_0 = h/(2e^2) = 12.9\,\text{k}\Omega$.

both materials far exceed the relevant excitation energies ($E, \Delta \ll E_F$), ensuring that the electron and reflected hole have nearly equal momenta.

AR is responsible for the finite subgap conductance in N-S junctions and forms the microscopic basis for all superconducting transport in mesoscopic contacts. At a single interface, it transfers one Cooper pair per reflection. When two superconductors are connected, successive Andreev processes give rise to discrete Andreev bound states in equilibrium and to multiple Andreev reflection under finite bias. The following sections build directly on this Andreev-based picture, developing ABS and MAR from the same underlying mechanism.

To make this qualitative picture quantitative and to calculate the corresponding I - V characteristics, we now turn to the Blonder–Tinkham–Klapwijk (BTK) model.

Blonder–Tinkham–Klapwijk Model

Building on the qualitative picture of Andreev reflection introduced above, the Blonder–Tinkham–Klapwijk (BTK) model provides a quantitative scattering description of an N-S interface with arbitrary transparency. It yields the energy-resolved probabilities for Andreev reflection (A), normal reflection (B), and transmission into the superconductor (C). The interface is represented by the dimensionless barrier strength Z , related to the normal-state transmission by

$$Z = \sqrt{1/\tau - 1}. \quad (72)$$

To incorporate finite quasiparticle lifetimes, we use the phenomenological broadening introduced by Pleceník *et al.*, replacing the quasiparticle energy by $E \rightarrow |E| + i\gamma$. This yields the modified coherence factors

$$u_0^2 = \frac{1}{2} \left(1 + \frac{\sqrt{(|E| + i\gamma)^2 - \Delta^2}}{|E| + i\gamma} \right), \quad v_0^2 = 1 - u_0^2. \quad (73)$$

Using the normalization factor d , the Andreev and normal reflection amplitudes (a, b) acquire the compact form,

$$\begin{aligned} A(E) &= aa^*, \quad a = u_0 v_0 / d, \quad d = u_0^2 + (u_0^2 - v_0^2) Z^2, \\ B(E) &= bb^*, \quad b = -(u_0^2 - v_0^2)(Z^2 + iZ)/d. \end{aligned} \quad (74)$$

For subgap energies, transmission into the quasi-particle continuum vanishes ($C \rightarrow 0$), so $A(E) + B(E) = 1$. It is therefore convenient to define the energy-resolved spectral weights ρ of the single-particle (1e) and two-particle (2e) processes,

$$\begin{aligned} \rho_{1e}(E) &= 1 - A(E) - B(E), \\ \rho_{2e}(E) &= 2 \cdot A(E), \end{aligned} \quad (75)$$

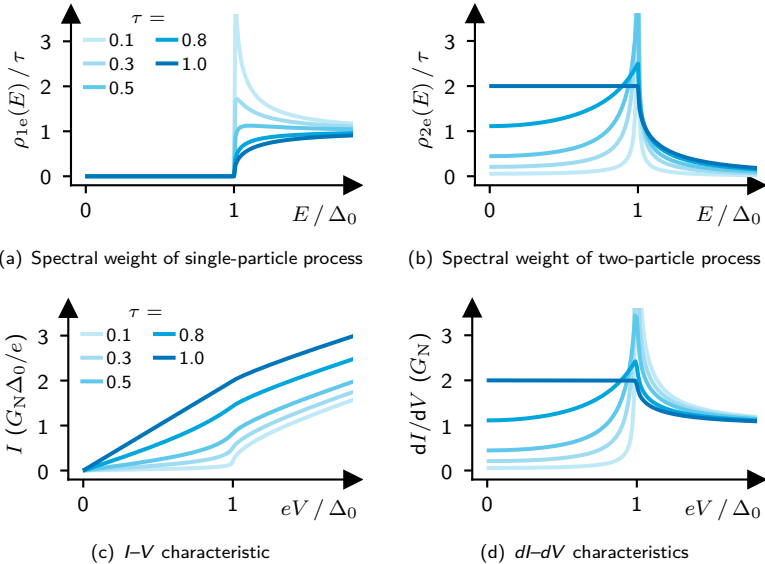


Figure 14 BTK spectral weights of the single-particle (1e) and two-particle (2e) channels and the corresponding I - V and dI - dV characteristics for various channel transparencies τ . Increasing τ shifts spectral weight from normal to Andreev processes, leading to enhanced subgap conductance and reduced coherence-peak height. Parameters correspond to aluminum (Eq. ??), with $T = 0$ and $\gamma = 0$.

which quantify the relative importance of normal and Andreev processes. Although these functions resemble densities of states, they should not be interpreted as the physical BCS DOS. Instead, they represent the BTK spectral kernels entering the current integral, shown in Fig. 14.

The current through an N-S junction then follows from the BTK kernel,

$$I_{\text{NS}}(V) = \frac{G_0}{e} \int_{-\infty}^{\infty} (\rho_{1e}(E) + \rho_{2e}(E)) (f(E) - f(E + eV)) \, dE. \quad (76)$$

yielding the I - V and dI - dV characteristics in Fig. 14. Increasing the transparency enhances the weight of Andreev processes, leading to a pronounced subgap conductance and a gradual reduction of the coherence-peak height. In the tunneling limit ($\tau \ll 1$), Eq. (76) reduces to the conventional quasiparticle-tunneling expression, while for $\tau \approx 1$ the transport approaches the Andreev limit, where charge is transferred predominantly in units of $2e$.

1.3.2 Andreev Bound States

Ambegaokar–Baratoff, Kulik–Omelyanchuk

$$I_C = \frac{\pi\Delta}{2e} G_N. \quad (77)$$

$$I_C R_N = \frac{\pi\Delta}{2e}. \quad (78)$$

$$I_C(T)R_N = \frac{\pi\Delta(T)}{2e} \tanh\left(\frac{\Delta(T)}{2k_B T}\right). \quad (79)$$

$$I(\varphi) = \frac{e\Delta}{\hbar} \frac{\tau \sin \varphi}{\sqrt{1 - \tau \sin^2(\varphi/2)}} \tanh\left(\frac{\Delta}{2k_B T} \sqrt{1 - \tau \sin^2(\varphi/2)}\right). \quad \tau \approx 1 \quad (80)$$

When two superconductors are connected through a short, phase-coherent constriction, the subgap spectrum is no longer continuous. Instead, coherent electron-hole trajectories become confined between successive Andreev reflections at the two superconducting interfaces. The resulting standing waves form discrete energy levels within the superconducting gap, known as Andreev bound states (ABS). These states constitute the fundamental microscopic origin of both the DC Josephson effect and the non-linear subgap transport observed at finite bias.

The physical mechanism underlying ABS formation can be understood from the Andreev reflection process introduced in Section 1.3.1. An electron entering the weak link from the left superconductor is retroreflected as a hole at the right interface, transferring a Cooper-pair into the right condensate. The hole then propagates back toward the left interface, where it undergoes a second Andreev reflection, converting back into an electron and transferring a second Cooper-pair to the left condensate. After these two reflections the system has returned to its original quasiparticle character, but the wavefunction has accumulated a phase. If the total phase gained over this round-trip is an integer multiple of 2π , the cycle interferes constructively, yielding a stationary, bound quasiparticle mode.

This quantization condition contains two contributions: (i) the Andreev reflection phase $\arccos(E/\Delta)$ acquired at each interface and (ii) the superconducting phase difference $\phi = \varphi_L - \varphi_R$ between the two electrodes. Solving the resulting phase-quantization condition leads to the characteristic energy–phase relation of a single transport channel with transmission τ ,

$$E_{\pm}(\phi) = \pm\Delta \sqrt{1 - \tau \sin^2\left(\frac{\phi}{2}\right)}. \quad (81)$$

Each channel supports a pair of particle-hole symmetric ABS, labeled by the signs \pm . The transmission τ governs the curvature of these levels: in the tunneling

limit ($\tau \ll 1$), the energies remain close to the gap edges ($E \approx \pm\Delta$), whereas for highly transparent channels ($\tau \approx 1$), the lower branch approaches zero energy at $\phi = \pi$. This dispersion encapsulates the essential physics of ballistic superconducting point contacts.

The bound states directly determine the phase-dependent supercurrent. At zero temperature, the negative branch $E_-(\phi)$ is occupied, and differentiation with respect to the phase yields

$$I(\phi) = \frac{2e}{\hbar} \frac{\partial E_-(\phi)}{\partial \phi} = \frac{e\Delta}{\hbar} \frac{\tau \sin \phi}{\sqrt{1 - \tau \sin^2(\phi/2)}}, \quad (82)$$

which is the current-phase relation (CPR) of a short Josephson junction with a single transport channel. For $\tau \ll 1$, this expression reduces to the sinusoidal CPR known from tunnel junctions. For $\tau \approx 1$, the CPR becomes strongly forward-skewed, reflecting the enhanced susceptibility of the ABS to changes in the superconducting phase.

Andreev bound states are not only responsible for the equilibrium supercurrent but also govern non-equilibrium transport at finite bias. When a DC voltage is applied across the junction, the superconducting phase evolves according to the Josephson relation,

$$\dot{\phi}(t) = \frac{2eV}{\hbar}, \quad (83)$$

rendering the ABS energies time-dependent. The bound states periodically traverse the superconducting gap, repeatedly crossing the continuum edges and allowing quasiparticles to enter or leave the ABS branches. This periodic population transfer gives rise to the highly non-linear subgap current known as multiple Andreev reflection (MAR), which is discussed in Section 1.3.3. In this sense, MAR can be interpreted as the dynamical evolution of the ABS spectrum under a linearly time-varying superconducting phase.

Finally, ABS play an increasingly important role in spectroscopic experiments on atomic contacts, proximitized nanowires, and Josephson quantum circuits. In these systems, ABS can be probed through microwave spectroscopy, quasiparticle injection, or gate-tunable transparency, and may serve as building blocks for novel qubit architectures. Their sensitivity to both phase and transmission makes them a uniquely versatile probe of mesoscopic superconductivity, bridging microscopic Bogoliubov quasiparticles and macroscopic Josephson dynamics within a single, unified framework.

fractional Shapiro Steps

1.3.3 Multiple Andreev Reflection

When two superconductors are connected through a constriction of atomic dimensions, the quasi-particle transport at subgap voltages is governed by multiple

Andreev reflection (MAR). In this regime, a quasi-particle incident on the interface cannot tunnel directly through the gap but undergoes successive Andreev reflections between the two superconducting electrodes. Each reflection converts an electron into a hole (or vice versa) while transferring a Cooper-pair to the condensate, effectively advancing the quasi-particle energy by eV with every traversal of the junction.

After m such reflections, the quasi-particle gains an energy of meV and can finally escape into the continuum when $meV = 2\Delta$, thus defining the characteristic subharmonic structure in the I - V curve. Distinct features appearing at

$$eV_m = \frac{2\Delta}{m}, \quad (m \in \mathbb{N}^+). \quad (84)$$

The process probability is given by

$$P_m \propto \tau^m, \quad (85)$$

what implies a unique I - V characteristics for each transmission. In the tunneling limit ($\tau \ll 1$), the subgap current is weak and dominated by single quasi-particle tunneling ($m = 1$). As the transmission increases, higher-order MAR processes become more pronounced, producing a series of peaks in the differential conductance. In the fully transparent limit ($\tau \approx 1$), these discrete features merge into a smooth subgap current approaching the Andreev limit, where transport becomes dominated by successive pair transfers rather than discrete tunneling events.

In contrast, multiple Andreev reflection cannot occur at a single N-S interface, since the normal electrode provides no second superconducting condensate to sustain repeated electron-hole conversions. After a single Andreev reflection, the reflected hole simply escapes into the normal reservoir instead of being reflected back toward the interface, limiting the process to one conversion event per incident quasi-particle.

Obtaining the I - V characteristics of multiple Andreev reflection (MAR) for arbitrary transmission represents a nontrivial problem, since the transport involves an infinite hierarchy of correlated two-particle processes occurring under nonequilibrium conditions. The first phenomenological descriptions were provided by BTK in 1982 and subsequently by Octavio et al. in 1983. These approaches treated MAR as a sequence of independent Andreev reflections within a semi-classical framework, successfully explaining the appearance of the subharmonic gap structure in the tunneling and weak-coupling limits. However, they relied on rate-equation or transmission-probability arguments and could not describe the full quantum coherence between successive reflections, nor the smooth crossover to the ballistic regime.

A major theoretical step forward was achieved by Cuevas, Martín-Rodero, and Levy Yeyati (1996, 1998), who developed a fully microscopic theory of MAR based on the nonequilibrium Keldysh Green's-function formalism. Their Hamiltonian approach (HA) treated the applied voltage self-consistently as a time-dependent phase $\phi(t) = \phi_0 + 2eVt/\hbar$, rendering the system periodic in time.

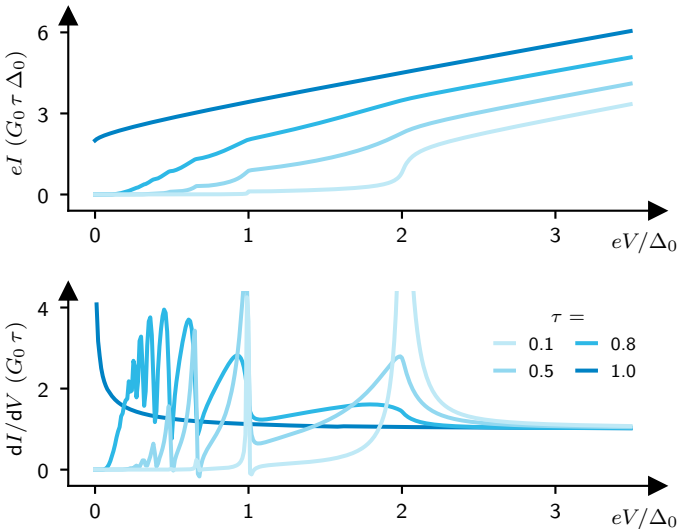


Figure 15 Numerical I - V and dI/dV characteristic calculated with the HA model by Cuevas ($\Delta_0 = 180 \mu\text{eV}$, $T = 0 \text{ K}$, $\gamma = 0$). The curves illustrate the smooth crossover between the tunneling regime ($\tau \ll 1$) and the Andreev limit ($\tau \approx 1$).

By solving this Floquet problem recursively, they obtained stationary solutions for the dc current that naturally include all orders of multiple Andreev reflections and remain valid for any channel transmission.

This formulation provides a continuous description linking the tunneling limit, where transport reduces to single-particle tunneling and reproduces the BCS density of states, with the fully transparent case, where coherent two-particle Andreev reflection dominates and yields a nearly linear subgap current. Intermediate transparencies show the gradual redistribution of spectral weight from the coherence peaks at the gap edge into the subgap region as successive Andreev processes become increasingly likely. This microscopic framework thus unifies the different transport regimes of superconducting point contacts within a single, quantitative model.

A further conceptual development was introduced through the framework of full counting statistics (FCS), which extends the microscopic MAR theory to include the entire probability distribution of transmitted charge. Instead of describing only the mean current, FCS characterizes the stochastic sequence of charge transfer events by introducing a counting field that tracks the passage of discrete charge quanta during a measurement interval. The resulting cumulant

generating function allows the evaluation of all current moments and cumulants, providing access to both the noise spectrum and higher-order correlations.

Within this picture, each MAR trajectory corresponds to the coherent transfer of a well-defined multiple of the electron charge, and the weight of each process is determined by its transmission dependent amplitude. This approach, pioneered by Belzig, Nazarov, and others, reveals that the subgap current in superconducting contacts is not continuous but built from discrete charge-transfer events whose effective charge increases as the bias is reduced. It thereby extends the Cuevas theory beyond the average current, offering a comprehensive, charge-resolved description of Andreev transport.

1.3.4 Photon-Assisted Multiple Andreev Reflection

Before discussing the effect of microwaves on multiple Andreev reflection (MAR), it is helpful to restate the two key mechanisms on which PAMAR is built. Photon-assisted tunneling (PAT), introduced in Section 1.1.4, arises whenever the applied voltage contains an AC component,

$$V(t) = V_{\text{dc}} + A \sin(2\pi\nu t), \quad (86)$$

which modulates the tunneling phase and generates a ladder of sidebands spaced by the photon energy $\hbar\nu$. [28] In contrast, MAR (Section 1.3.3) describes the coherent motion of a quasiparticle that undergoes m Andreev reflections between two superconductors, gaining energy eV on each traversal until $meV = 2\Delta$. [Cuevas1996, Cuevas1998] Each MAR trajectory corresponds to the transfer of an effective charge

$$q_m = me, \quad (87)$$

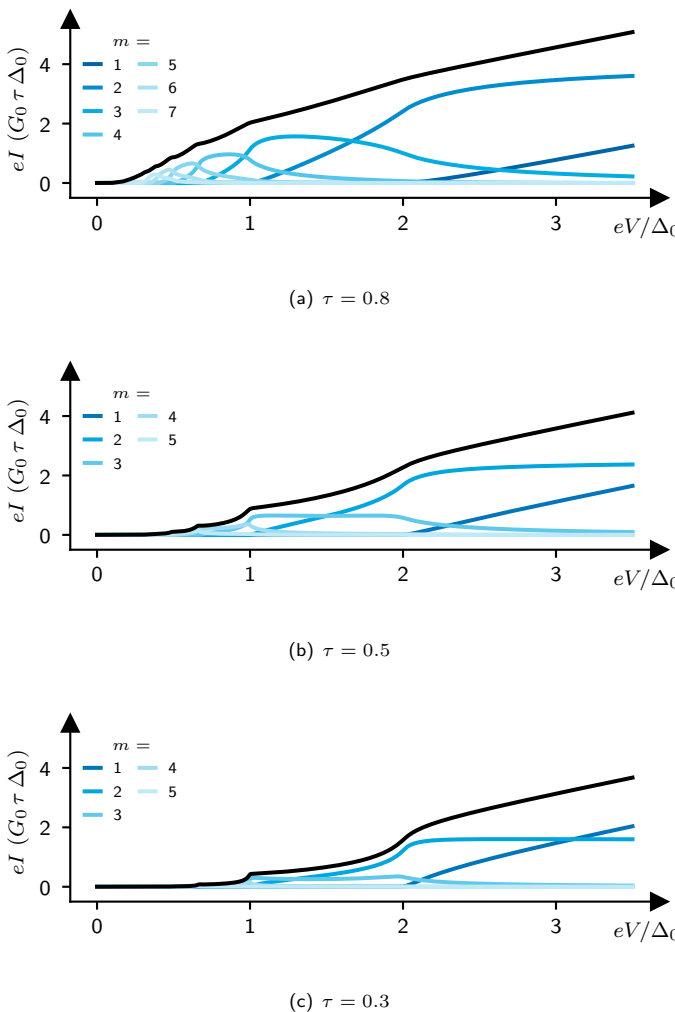
and the subgap current is a weighted sum of these elementary charge-transfer processes.

When an AC voltage is applied, the coherent MAR trajectories remain operative, but the time dependence of Eq. (86) introduces an oscillatory phase into each order- m process. For a MAR trajectory transferring the charge q_m , the superconducting phase difference becomes

$$\phi_m(t) = \phi_0 + \frac{q_m V_{\text{dc}}}{\hbar} t - \alpha_m \cos(2\pi\nu t), \quad \alpha_m = \frac{q_m A}{\hbar\nu}. \quad (88)$$

The modulation amplitude α_m increases linearly with the effective charge q_m , implying that higher-order MAR processes couple more strongly to microwave irradiation. This reflects that MAR transfers multiple electron charges in a single coherent sequence; the entire string of reflections is phase-modulated as a whole.

The time-periodic phase renders the Hamiltonian a Floquet problem, as already discussed in the microscopic MAR theory of Cuevas *et al.* [Cuevas1996,

**Figure 16** Gesamtbeschriftung der Figur.

Cuevas1998] Expanding $e^{i\phi_m(t)}$ into its Fourier components gives

$$e^{i\phi_m(t)} = \sum_{n=-\infty}^{\infty} J_n(\alpha_m) \exp\left[i\left(\frac{q_m V_{dc}}{\hbar} + n2\pi\nu\right)t\right], \quad (89)$$

revealing that each MAR trajectory generates a ladder of photon-dressed sidebands. The Bessel function $J_n(\alpha_m)$ is the amplitude to absorb or emit n photons, and the observable current depends on the probability $J_n^2(\alpha_m)$ of occupying the corresponding Floquet mode. [kot, 28] This mechanism is identical to PAT but extended to charge-transfer processes of arbitrary order m .

Averaging the microscopic current operator over one period of the drive yields a charge-resolved generalization of the Tien–Gordon expression,

$$I(V_{dc}, A) = \sum_{m=1}^{\infty} \sum_{n=-\infty}^{\infty} J_n^2(\alpha_m) I_m\left(V_{dc} - \frac{n\hbar\nu}{q_m}\right), \quad (90)$$

where $I_m(V)$ denotes the DC MAR contribution of order m in the absence of irradiation. Equation (90) is the *unified, charge-resolved Tien–Gordon formula* for superconducting point contacts. It shows that microwaves do not alter the internal structure of MAR—as captured by $I_m(V)$ —but merely generate shifted replicas of each MAR trajectory spaced by $\pm n\hbar\nu/q_m$. The strength of each replica is determined by α_m and thus grows with the MAR order.

The resulting I – V characteristics display a hierarchy of photon-assisted features at

$$eV_{m,n} = \frac{2\Delta}{m} \pm \frac{n\hbar\nu}{m}, \quad (91)$$

corresponding to the intersections of the MAR thresholds with the photon sidebands. Changing the microwave frequency controls the spacing of these replicas, while changing the amplitude redistributes spectral weight among them. All structures occur at finite bias and arise from quasiparticle dynamics, distinguishing PAMAR from the Shapiro effect (Section 1.2.2), which originates from phase locking in the zero-bias Josephson regime and follows a different (non-Tien–Gordon) mechanism.

This framework naturally unifies photon-assisted transport across normal, N–S, and S–S junctions. PAT corresponds to the $m = 1$ single-electron process ($q_1 = e$). PAAR at an N–S interface arises from the $m = 1$ and $m = 2$ channels ($q_1 = e, q_2 = 2e$). PAMAR includes the entire hierarchy $q_m = me$ associated with MAR. Thus, the charge-resolved Tien–Gordon formalism provides a single, conceptually transparent mechanism describing PAT, PAAR, and PAMAR within the same theoretical structure, differing only by the effective charge transferred in the underlying microscopic process.

1.4 Stochastic Description

In the previous sections superconducting transport was described in three complementary ways. The microscopic picture treats it as incoherent quasiparticle tunneling, the macroscopic picture describes it as coherent Cooper-pair dynamics governed by the superconducting phase, and the mesoscopic picture considers coherent electron-hole processes in high-transmission weak links. All of these descriptions rely on a well-defined superconducting phase and on the coherence of successive tunneling events. When the electromagnetic environment generates strong voltage fluctuations, this phase coherence is lost. The junction then enters the stochastic transport regime.

In the stochastic regime, the loss of phase coherence plays a central role. The superconducting phase ϕ is conjugate to the charge Q on the junction,

$$[\phi, Q] = 2e\dot{i}, \quad (92)$$

implying that a well-defined phase requires charge to be delocalized, whereas localized charge leads to strong phase fluctuations. Any electromagnetic environment connected to the junction produces voltage fluctuations $\delta V(t)$, which translate into fluctuations of the phase via the AC Josephson relation (Eq. 54),

$$\delta\phi(t) = \frac{2e}{\hbar} \int_0^t \delta V(t') dt'. \quad (93)$$

Large phase fluctuations randomize the phase so strongly that the average of the phase-dependent factor vanishes

$$\langle \exp(i\phi(t)) \rangle = 0. \quad (94)$$

This loss of a non-zero phase average signals the destruction of long-range phase coherence. Consequently, the coherent Josephson effect, Andreev bound states, and multiple Andreev reflections no longer exist. Transport becomes a sequence of incoherent tunneling events whose rates are governed by the energy exchanged with the electromagnetic environment. The crossover between coherent and incoherent regimes is controlled by the strength of the environment. Weak damping ($\text{Re } Z(\omega) \ll R_Q$) preserves phase coherence, whereas strong damping ($\text{Re } Z(\omega) \sim R_Q$) leads to phase diffusion and marks the onset of the stochastic transport regime.

So, charge transfer no longer proceeds through coherent condensate dynamics or well-defined quasiparticle trajectories, but instead through discrete and statistically independent tunneling events. The electromagnetic environment can absorb or emit energy during each event, so that tunneling rates are determined not only by the electronic density of states but also by the impedance of the surrounding circuit. This interplay is captured by the $P(E)$ -theory, which provides the universal framework for describing energy exchange between a tunnel junction and its environment.

The stochastic description therefore complements the microscopic, macroscopic, and mesoscopic frameworks by covering the fully incoherent limit of superconducting transport. The following sections introduce the origin of phase fluctuations, the $P(E)$ -formalism, and the resulting phenomena: dynamical Coulomb blockade of single-electron tunneling⁸, incoherent Cooper-pair tunneling and its photon-assisted counterpart, incoherent Andreev reflection in the absence of phase coherence, and finally the superconducting single-electron transistor as a device in which these processes combine in a controlled and experimentally relevant manner.

1.4.1 $P(E)$ -Theory

In the presence of strong phase fluctuations, charge transport through a junction occurs as a sequence of independent tunneling events. Because the electromagnetic environment can absorb or emit energy during such a process, the tunneling rate is determined not only by the electronic density of states but also by the probability $P(E)$ that the environment exchanges an energy E with the junction. This renders the tunneling process inelastic even at zero temperature and forms the basis of the stochastic description of superconducting transport.

The statistical properties of these fluctuations are determined by the environmental impedance $Z(\omega)$. Within linear-response theory, the phase correlation function can be written as

$$J(t) = \frac{2}{R_Q} \int_0^\infty \frac{\text{Re } Z(\omega)}{\omega} \coth\left(\frac{\hbar\omega}{2k_B T}\right) (\cos(\omega t) - 1) - i \sin(\omega t) d\omega, \quad (95)$$

where R_Q is the superconducting resistance quantum⁹.

The structure of Eq. 95 reflects how the electromagnetic environment shapes the phase dynamics. The factor $\text{Re } Z(\omega)$ captures the dissipative part of the environment, which determines how strongly voltage fluctuations couple to the junction. It appears divided by ω because the phase is the time integral of the voltage, so that low-frequency components contribute most strongly to its fluctuations. The thermal occupation of each environmental mode enters through the factor $\coth(\beta\hbar\omega/2)$, ensuring that both quantum and thermal noise are included. The combination $\cos(\omega t) - 1$ forms the real part of $J(t)$ and describes phase

⁸In the microscopic description, tunneling is elastic and proceeds between well-defined BCS quasi-particle states, which we refer to as quasi-particle tunneling. In contrast, the stochastic description considers single-electron tunneling events dressed by environmental fluctuations, where energy exchange with the environment renders the process inelastic and probabilistic.

⁹The superconducting resistance quantum is $R_Q = h/(2e)^2 \approx 6.453 \text{ k}\Omega$, which appears when phase fluctuations couple to Cooper-pair charge $2e$. The quantity $R_0 = h/2e^2 = 12.9 \text{ k}\Omega$ is the resistance quantum for a single spin-resolved electronic channel. In this thesis the conductance quantum is defined as $G_0 = 2e^2/h = 77.48 \mu\text{S}$, which includes spin degeneracy and corresponds to the conductance of a fully transmitting normal-state channel. R_Q governs the strength of phase fluctuations in the stochastic description, while R_0 and G_0 appear in mesoscopic transport and Landauer-type expressions.

diffusion, reflecting the loss of phase memory induced by fluctuating voltages. In contrast, the term $-i \sin(\omega t)$ yields the imaginary part of $J(t)$ and encodes the phase winding generated by the environment. Altogether, these ingredients ensure that the long-time or low-frequency behavior of the environmental impedance dominates the asymptotic form of $J(t)$.

The function $P(E)$ is defined as the Fourier transform of $J(t)$,

$$P(E) = \frac{1}{2\pi\hbar} \int_{-\infty}^{\infty} \exp(J(t) + iEt/\hbar) dt. \quad (96)$$

This formulation relies on the assumption of a linear, Gaussian environment, so that all phase fluctuations are fully captured by the correlator $J(t)$. The shape of $P(E)$ therefore reflects the spectral properties of the environment in a universal way.

An important universal property of the $P(E)$ function is its normalization,

$$\int_{-\infty}^{\infty} P(E) dE = 1, \quad (97)$$

which follows directly from the definition in Eq. 96 and the condition $J(t \rightarrow 0) = 0$. This ensures that environmental fluctuations redistribute spectral weight among different energy-exchange channels without altering the total tunneling probability.

In thermal equilibrium the environment additionally satisfies the detailed-balance relation

$$P(-E) = e^{-E/k_B T} P(E), \quad (98)$$

which guarantees thermodynamic consistency of energy exchange processes.

The rate for a tunneling event¹⁰,

$$\Gamma(V) = \int_{-\infty}^{\infty} P(E) F(E, V) dE, \quad (99)$$

is obtained from Fermi's golden rule as a convolution of $P(E)$ with the electronic part of the problem $F(E, V)$. It collects the relevant density of states and Fermi functions. This expression is completely general and applies to single-electron tunneling, Cooper-pair tunneling, and Andreev processes alike¹¹.

Several limiting forms of $P(E)$ are particularly useful for understanding the stochastic transport regime. The $P(E)$ -framework applies strictly to tunneling processes, where individual transfer events are well separated and described by

¹⁰Throughout this work we distinguish between the Dynes broadening parameter γ , which enters the quasi-particle density of states in the microscopic tunneling description, and the tunneling rates Γ that appear in the stochastic description of incoherent charge transfer. The two quantities are unrelated and refer to different physical mechanisms.

¹¹The only distinction is the transferred charge q in a tunneling event. The environment couples to the energy qV , with $q = e$ for single-electron tunneling and $q = 2e$ for Cooper-pair tunneling and Andreev reflection.

Fermi's golden rule. It does not capture coherent multi-particle trajectories such as multiple Andreev reflections, which require a mesoscopic description and finite transparency. For a weak electromagnetic environment with, phase fluctuations are small and $P(E)$ becomes sharply peaked around $E = 0$, approaching

$$P(E) \approx \delta(E) \quad (\text{Re } Z(\omega) \ll R_Q). \quad (100)$$

In this limit tunneling is effectively elastic and coherent transport is recovered.

In contrast, a strong electromagnetic environment with $\text{Re } Z(\omega) \sim R_Q$ produces large phase fluctuations and a broad $P(E)$, such that tunneling events must exchange energy with the environment. This regime marks the onset of incoherent, environment-assisted charge transfer and underlies phenomena such as dynamical Coulomb blockade and incoherent Cooper-pair tunneling.

For an Ohmic environment, the low-energy behavior of $P(E)$ exhibits a universal power law,

$$P(E) \propto E^{2R/R_Q - 1} \quad (E > 0, \text{Re } Z(\omega) = R), \quad (101)$$

which reflects the suppression of small-energy exchange by quantum fluctuations. This result follows from the low-frequency limit of an environment with a frequency-independent real impedance, $\text{Re } Z(\omega) = R$, and is therefore a property of the $P(E)$ kernel itself rather than a feature of any specific transport process.

The specific consequences of these limiting forms for single-electron tunneling, Cooper-pair tunneling, and subgap Andreev processes are discussed in the subsequent sections.

1.4.2 Dynamical Coulomb Blockade

Dynamical Coulomb blockade (DCB) describes the suppression of single-electron tunneling at low bias due to the combined effects of charge quantization and the electromagnetic environment. In contrast to the microscopic description, where quasi-particle tunneling is elastic and governed solely by the electronic density of states, DCB arises when the environment possesses a sufficiently large real impedance such that the transfer of an electron across the junction requires the environment to absorb a finite amount of energy. If this energy is not available, the tunneling event is suppressed.

The physical origin of dynamical Coulomb blockade can be understood by considering the energetic requirements of a single tunneling event. When an electron traverses the junction, it must transiently raise the voltage across the junction capacitor, which requires an electrostatic energy of the order of $E_C = e^2/2C$. Because this charge transfer takes place within a quantum circuit, the required energy cannot arise from the junction itself, but must instead be supplied by the surrounding electromagnetic environment. Whether the environment can

provide this energy is determined by the probability distribution $P(E)$, whose low-energy weight reflects the extent to which environmental modes can exchange small amounts of energy.

If the real part of the environmental impedance is appreciable at low frequencies, the corresponding suppression of $P(E \approx 0)$ makes it unlikely that the environment can provide the small energy quanta required for low-energy tunneling processes. This not only reduces the differential conductance near zero voltage but more generally suppresses all tunneling events that rely on small energy exchange with the environment. The resulting modification of the I - V characteristics is therefore governed entirely by the low-frequency properties of the impedance. This mechanism, rooted in the discrete transfer of charge across the junction and the energetic constraints imposed by the environment, captures the universal and model-independent essence of dynamical Coulomb blockade.

Whenever the low-frequency part of the environmental impedance is Ohmic, $\text{Re } Z(\omega) = R$ for $\omega \ll \omega_c$, the suppression of small-energy exchange produces a characteristic power-law dependence of the differential conductance,

$$\frac{dI(V)}{dV} \propto V^{2R/R_Q} \quad (eV \ll \hbar\omega_c), \quad (102)$$

where ω_c denotes the effective high-frequency cutoff of the environment. For a simple RC model one obtains $\omega_c = 1/RC$, but in general ω_c is set by the fastest environmental mode for which the Ohmic approximation remains valid. This "zero-bias anomaly" directly reflects the low-energy behavior of $P(E)$ and constitutes the most prominent experimental signature of DCB. While Eq. 102 applies to a purely Ohmic environment, a zero-bias suppression of the conductance is a generic feature whenever the low-frequency part of the environmental impedance provides dissipation, i.e. whenever $\text{Re } Z(\omega \rightarrow 0) > 0$. In this case $P(E \rightarrow 0) \rightarrow 0$ and a zero-bias anomaly emerges with an exponent determined by the low-frequency behavior of $\text{Re } Z(\omega)$.

For environments with a real impedance that exceeds R_Q at low frequencies the tunneling electron cannot draw the small amounts of energy needed for charge transfer. The conductance then becomes exponentially small at low bias. In this strong damping limit the charge remains localized on the junction capacitor and the junction behaves as an effective insulator¹².

DCB is not restricted to normal-metal junctions. The expression for the tunneling current remains

$$I(V) \propto \int_{-\infty}^{\infty} P(E) \frac{N_1(E)}{N_0} \frac{N_2(E + eV)}{N_0} (f_1(E) - f_2(E + eV)) dE. \quad (103)$$

¹²This localization is reminiscent of Anderson localization but the underlying mechanism is different. Anderson localization relies on interference of many spatial paths, whereas the localization in dynamical Coulomb blockade arises from strong phase fluctuations generated by the environment, which destroy coherence and prevent the electron from accessing low energy exchange channels. cite: **Anderson, Schertel**

but the electronic factor inherits the density of states of the electrodes. For NN junctions the density of states is constant, for NS junctions it contains the superconducting BCS form on one side, and for SS junctions both electrodes contribute superconducting densities of states. Regardless of the microscopic details, the environment always suppresses single-electron tunneling at low bias through the same mechanism. In SIS junctions the single-electron current appears only above the pair-breaking threshold $eV \gtrsim 2\Delta$, but once quasi-particle states are available, the environmental suppression of small-energy exchange acts on the onset in the same universal manner.

We now apply this general formalism to single-electron tunneling before turning to the corresponding two-electron processes.

Dynamical Coulomb Blockade with Environmental Resonances

If the impedance contains discrete resonances that originate from inductive elements or cavity modes, the real part of the impedance acquires sharp features at the corresponding frequencies. These features imprint themselves onto the $P(E)$ function, which develops peaks at the energies of the environmental modes. The resulting $I(V)$ curves contain satellite structures at the same energies. These resonant features arise purely from the structure of the electromagnetic environment and should not be confused with photon-assisted dynamical Coulomb blockade, discussed below, which requires an externally applied microwave drive and produces sidebands at integer multiples of the drive frequency.

A discrete environmental resonance at frequency ω_0 produces a characteristic structure in the $P(E)$ function. The oscillatory contribution to the phase correlator leads to a Poisson series of sidebands in the energy-exchange probability,

$$P(E) = e^{-\alpha_0} \sum_{n=0}^{\infty} \frac{\alpha_0^n}{n!} P_{\text{Ohmic}}(E - n\hbar\omega_0), \quad (104)$$

where $\alpha_0 = R/R_Q$ quantifies the coupling strength to the mode. Each term represents the absorption or emission of n quanta of the environmental resonance. The measurable current inherits the same structure through the convolution with the electronic factor,

$$I(V) = e^{-\alpha_0} \sum_{n=0}^{\infty} \frac{\alpha_0^n}{n!} I_0\left(V - \frac{n\hbar\omega_0}{e}\right), \quad (105)$$

so that satellite peaks appear at voltages shifted by $n\hbar\omega_0/e$. These features arise solely from the internal mode of the environment and do not require an external microwave drive.

Photon-Assisted Dynamical Coulomb Blockade

In the presence of microwave irradiation, a tunneling electron may absorb or emit integer multiples of the photon energy $h\nu$. In the stochastic regime this photon-assisted tunneling does not arise from a coherent phase modulation as in the Tien–Gordon description, but instead from additional energy channels in the inelastic $P(E)$ -process. In this regime the microwave field is treated as a classical, deterministic voltage modulation superposed on the stochastic environmental fluctuations; no phase-coherent mixing between sidebands occurs. The classical treatment of the microwave field is valid whenever the applied drive contains many photons per cycle, such that quantum fluctuations of the field are negligible compared to the deterministic modulation.

A tunneling event may therefore exchange an energy $nh\nu$, with both the environment and the microwave field. The corresponding probability is obtained by dressing the environmental probability with Bessel weights,

$$P(E) = \sum_{n=-\infty}^{\infty} J_n^2 \left(\frac{eA}{h\nu} \right) P_0(E - nh\nu), \quad (106)$$

where A and ν are the amplitude and frequency of the applied microwave drive.

The resulting photon-assisted DCB current generalizes Eq. 103 by incorporating the additional photon sidebands,

$$I(V_0) = \sum_{n=-\infty}^{\infty} J_n^2 \left(\frac{eA}{h\nu} \right) \cdot I_0 \left(V_0 - \frac{nh\nu}{e} \right). \quad (107)$$

Photon-assisted DCB therefore combines environmental energy exchange with photon-assisted processes in a fully incoherent manner. In contrast to coherent PAT in the microscopic Tien–Gordon picture, no phase-coherent sideband mixing occurs. Instead, microwaves redistribute weight among the inelastic channels of the $P(E)$ kernel. This produces microwave-induced replicas of the DCB-suppressed current without generating coherent Shapiro-like features.

DCB constitutes the single-electron $q = e$ counterpart of incoherent Cooper-pair tunneling, which is discussed next. Whereas DCB suppresses the tunneling of individual electrons, the same environmental interaction enables incoherent $q = 2e$ charge transfer in superconducting junctions. This forms the basis of incoherent Cooper-pair tunneling, discussed in the following section.

1.4.3 Incoherent Two-Electron Tunneling

In the stochastic regime, the superconducting phase becomes fully randomized by the electromagnetic environment, and any phase-coherent mechanism Josephson tunneling, Andreev bound states, and multiple Andreev reflections is suppressed.

Nevertheless, the transfer of a charge ($2e$) across a voltage-biased junction remains possible through inelastic, stochastic tunneling events. These processes form a unified class of incoherent two-electron tunneling, in which the junction exchanges an energy ($2e$) V with its environment. Their rates are governed by the same $P(E)$ kernel as in dynamical Coulomb blockade, but evaluated at the doubled energy scale associated with the transferred charge.

Despite their different microscopic origins, incoherent Cooper-pair tunneling (SS junctions) and incoherent Andreev reflection (NS junctions) share the same universal structure:

$$\Gamma_{2e}(V) = \int_{-\infty}^{\infty} P(E) F_{2e}(E, V) dE, \quad (108)$$

with the environment coupling to the charge ($2e$) through the argument of the $P(E)$ function. The only distinction lies in the electronic prefactor $F_{2e}(E, V)$, which encodes the microscopic structure of the junction.

The stochastic regime treats all ($2e$) processes on equal footing: both incoherent Cooper-pair tunneling in SS junctions and incoherent Andreev reflection in NS junctions are described by the same charge- $(2e)$ energy-exchange kernel $P(E)$, with only their electronic prefactors differentiating them. The following subsections describe these two cases in detail.

Incoherent Cooper-Pair Tunneling

In a SS tunnel junction the coherent Josephson effect is destroyed once environmental phase fluctuations become strong enough that the phase-dependent part of the Cooper-pair tunneling amplitude averages to zero

$$\langle \exp(i\phi(t)) \rangle = 0. \quad (109)$$

The Josephson coupling energy $E_J = \hbar I_C/2e$ then no longer produces a DC supercurrent but enters the tunneling rate in second order. Since a Cooper pair of charge ($2e$) is transferred between the two condensates, the corresponding electronic factor takes the simple form

$$F_{\text{ICPT}}(E, V) = \frac{\pi E_J^2}{2\hbar} (\delta(E - 2eV) - \delta(E + 2eV)), \quad (110)$$

which, inserted into Eq. 108, yields the standard expression for the incoherent Cooper-pair tunneling rate and by multiplying by the transferred charge gives the ICPT current,

$$I_{\text{ICPT}}(V) = \frac{\pi E_J^2}{\hbar} (1 - \exp(-2eV/k_B T)) P(2eV). \quad (111)$$

The low-bias suppression of $I_{\text{ICPT}}(V)$ is therefore entirely governed by the behavior of $P(E)$ near $E = 0$. For Ohmic environments this leads to the universal power law $I \propto V^{2R/R_Q-1}$, identical to the dynamical Coulomb blockade of single-electron tunneling but evaluated at the doubled charge ($2e$).

Incoherent Andreev Reflection

At an NS interface, subgap transport is governed microscopically by Andreev reflection: an incoming electron from the normal electrode is retroreflected as a hole, while a Cooper pair is injected into the superconductor. In the coherent BTK description this process relies on well-defined electron-hole amplitudes. Once environmental phase fluctuations destroy coherence, Andreev reflection remains possible but becomes a stochastic, inelastic two-electron tunneling process.

In the tunneling limit, the coherent BTK structure collapses to a single effective second-order tunneling parameter, and the electronic factor becomes

$$F_{\text{IAR}}(E, V) = \frac{\tau^2 G_0}{e^2} (f(E - eV) - f(E + eV)) , \quad (112)$$

where $f(E)$ is the Fermi function of the normal electrode. Inserting Eq. 112 into the general 2e formula 108 results in the corresponding current,

$$I_{\text{IAR}}(V) = \frac{2\tau^2 G_0}{e} \int_{-\infty}^{\infty} P(E) (f(E - eV) - f(E + eV)) dE . \quad (113)$$

As in ICPT, low-bias IAR is suppressed by $P(E \rightarrow 0)$. The only difference between IAR and ICPT lies in the electronic factor: the normal metal provides the Fermi functions $f(E \pm eV)$, whereas ICPT involves only the condensate wave functions encoded in E_J^2 .

Finally, it is important to clarify why neither coherent Andreev reflection nor multiple Andreev reflections survive in a SS junction once the system enters the stochastic regime. In an SS junction both electrodes possess gapped BCS densities of states, so no normal-metal continuum is available to support elastic electron-hole conversion inside the gap. Coherent Andreev reflection relies on well-defined electron and hole amplitudes with a fixed superconducting phase, and multiple Andreev reflections require an extended sequence of such coherent conversions. Strong environmental phase fluctuations destroy this phase coherence, making the amplitudes of successive conversion events uncorrelated. As a result, MAR processes are fully suppressed, and even single Andreev reflection has no independent meaning in SS junctions. The only remaining subgap transport channel is therefore the incoherent transfer of a Cooper pair between the two condensates, described by incoherent Cooper-pair tunneling (ICPT).

Photon-Assisted Incoherent Two-Electron Tunneling

When a microwave drive is applied, the phase remains fully randomized by the environment, so no Shapiro-like coherent interference occurs. Instead, the drive opens additional inelastic channels. The probability to exchange energy with

both environment and microwave field becomes

$$P(E) = \sum_{n=-\infty}^{\infty} J_n^2 \left(\frac{2eA}{h\nu} \right) P_0(E - n\hbar\nu). \quad (114)$$

Inserting Eq. 114 into the 2e tunneling rate yields the photon-assisted current,

$$I_{2e}(V_0) = \sum_{n=-\infty}^{\infty} J_n^2 \left(\frac{2eA}{h\nu} \right) I_{2e,0} \left(V_0 - \frac{n\hbar\nu}{2e} \right), \quad (115)$$

where $I_{2e,0}(V)$ is either Eqs. 111 (ICPT) or 113 (IAR), depending on the junction type. Thus photon-assisted ICPT and photon-assisted IAR share the same structure, only their electronic prefactors differ.

1.4.4 Superconducting Single-Electron Transistor

The superconducting single-electron transistor (SSET) combines two fundamental ingredients of mesoscopic charge transport: Coulomb blockade due to charge quantization on a small island, and superconductivity in the source, drain, and island electrodes. To understand its transport characteristics, it is instructive to first recall the basic concepts of static Coulomb blockade and the operation of a normal-state single-electron transistor (SET), before discussing the qualitative differences that arise once all electrodes are superconducting.

Static Coulomb Blockade

When a metallic island is isolated by tunnel junctions of capacitance C_1 and C_2 , adding an excess electron requires the electrostatic charging energy

$$E_C = e^2 / (2C_\Sigma), \quad C_\Sigma = C_1 + C_2 + C_G \quad (116)$$

where C_G denotes the gate capacitance.

For the static Coulomb blockade, one need to suppress both, thermal and charge fluctuation. Thermal fluctuation are suppressed, when the charging energy exceeds the thermal energy $E_C \gg k_B T$. Charge Fluctuations are considered to be suppressed usually, when the normal state tunneling resistance exceed the resistance quantum $R_T \gg R_Q$. Only when both criteria are met does the island retain a well-defined integer charge. Adding or removing an electron is both energetically unfavorable and quantum-mechanically unlikely. In this regime charge becomes localized on the island.

This suppression of charge motion is known as static Coulomb blockade. The island is then characterized by well-defined charge states ne and its electrostatic energy

$$E_n(V_G) = E_C(n - n_G)^2, \quad (117)$$

with $n_G = C_G V_G / e$ the dimensionless gate-induced charge. Degeneracy between two charge states occurs at half-integer values of n_G .

Normal-State SET

A normal-state single-electron transistor consists of two tunnel junctions in series, each with tunneling resistance $R_{T,i}$ and capacitance C_i , and a metallic island between them. Transport occurs through sequential single-electron transitions $n \rightarrow n \pm 1$ whenever the electrostatic energy decreases during the tunneling event.

Instead of writing the general condition $\Delta E < 0$, it is more transparent to express the onset of conduction directly through the Coulomb-diamond boundaries. The island has electrostatic energy $E_n = E_C(n - n_g)^2$, and a tunneling transition becomes energetically allowed when the applied bias provides enough energy to overcome the charging cost. This yields the diamond edges

$$|eV| = 2E_C |2n_g - (2n + 1)|, \quad (118)$$

which delimit regions of blocked and allowed transport in the (V, V_g) plane. Inside these diamonds no sequential tunneling is possible and the SET is in Coulomb blockade; on the diamond edges, the charge states n and $(n \pm 1)$ become degenerate, giving rise to conductance peaks; and outside the diamonds sequential single-electron tunneling provides a finite conductance.

Outside the Coulomb-blockaded region the SET behaves as two independent tunnel junctions in series. The sequential-tunneling conductance therefore approaches $G_{\text{seq}} = (R_{T,1} + R_{T,2})^{-1}$, which reduces to $G_T/2$ for symmetric junctions.

Away from the degeneracy points, only higher-order cotunneling processes remain, and the conductance is strongly suppressed.

Superconducting SET (SSET): Why It Is Special

When the leads and the island become superconducting, the SET acquires qualitatively new transport channels:

1. **Cooper-pair tunneling** allows $2e$ charge transfer between neighboring charge states $n \rightarrow n \pm 2$. In the absence of phase coherence (as treated in this chapter), these processes occur as incoherent Cooper-pair tunneling (ICPT) with rates governed by the same $P(E)$ kernel that enters single-junction ICPT.
2. **Quasiparticle tunneling** becomes possible only above the superconducting energy gap. Single-electron transitions $n \rightarrow n \pm 1$ require an energy cost of at least Δ per broken pair, modifying the Coulomb blockade diagram into superconducting Coulomb diamonds.

3. **Parity effects** arise because the island prefers to host an even number of electrons. Near charge degeneracy, odd charge states acquire an additional energy cost of Δ , which modifies the periodicity of the stability diagram and the accessible charge states at low temperature.

Together, these ingredients produce a device whose transport is governed not simply by sequential tunneling, but by competing single-electron and two-electron processes, each dressed by the electromagnetic environment through stochastic energy exchange. The SSET therefore naturally combines all mechanisms introduced in this chapter: DCB of quasiparticles, incoherent Cooper-pair tunneling, and incoherent Andreev processes at the NS interfaces between island and leads.

Transport Cycles in the SSET

The coexistence of quasiparticle and Cooper-pair processes gives rise to distinct transport cycles, the most prominent being the Josephson-quasiparticle (JQP) cycle, the double Josephson-quasiparticle (DJQP) cycle, and subgap cycles involving incoherent Andreev reflection. These cycles arise when a sequence of energetically allowed transitions forms a closed loop in the (n, V) plane, enabling a steady-state current through the device. In the stochastic regime, the rates of the Cooper-pair steps are governed by ICPT, the quasiparticle steps follow the DCB-modified single-electron tunneling expression, and the cycle current is set by the slowest transition.

A quantitative description is obtained by writing rate equations for the charge-state occupations and computing the steady-state current, discussed in the following sections.

Coherent Multiple Andreev Reflections in SSETs

In addition to incoherent processes described by the $P(E)$ -framework, superconducting single-electron transistors can access a qualitatively different regime in which transport is governed by coherent multiple Andreev reflections (MAR). This regime appears when the electromagnetic environment is weak and the junction transparencies are sufficiently large so that the superconducting phase remains well defined over many successive electron-hole conversion events.

In a superconducting weak link with transmission $\tau \lesssim 1$, an electron incident at subgap energy undergoes repeated Andreev reflections at the two NS interfaces. These coherent trajectories gain energy in steps of eV and allow charge transfer at bias voltages $eV < 2\Delta$. The resulting MAR current produces characteristic subharmonic gap structures at

$$eV = \frac{2\Delta}{n}, \quad n = 1, 2, 3, \dots$$

which appear as step-like onsets in the current-voltage characteristics and as pronounced lines of enhanced conductance in the SSET stability diagram.

Experimental observations (Lorenz and Sprenger).

Coherent MAR in aluminium SSETs was first observed in detail by Lorenz [[LorenzPhD](#)] and Sprenger [[SprengerPhD](#)]. Their devices featured moderately transparent tunnel junctions and an electromagnetic environment with low dissipation, allowing the phase to remain coherent over several Andreev cycles. Both theses report clear subharmonic gap structure, MAR-induced steps in the $I(V)$ characteristics, and coherent interference features indicative of well-preserved superconducting phase dynamics.

Theoretical and hybrid-regime simulations (Sobral-Rey).

More recently, Sobral-Rey extended this picture by studying the interplay of MAR and Coulomb blockade in hybrid SSET devices in a regime that interpolates between pure tunneling and coherent Andreev transport. Her simulations and measurements [[SobralReyPRL2024](#)] demonstrate how MAR survives in the presence of charging effects, how Coulomb blockade modifies the MAR subharmonic structure, and how the onset of higher-order MAR processes depends sensitively on junction transparency, parity effects, and the detuning from charge degeneracy. These results show that MAR remains robust well beyond the simplest weak-coupling limit and that charging energy and superconductivity can coexist in a nontrivial way in the intermediate-transparency regime.

Relation to the stochastic regime.

Coherent MAR processes rely on a well-defined superconducting phase and on the correlated nature of successive electron-hole conversions. Therefore, they lie fundamentally outside the applicability of the $P(E)$ -framework, which assumes statistically independent tunneling events. As environmental damping increases or the junction transparency is reduced, phase fluctuations destroy this coherence and MAR gradually gives way to incoherent two-electron processes (ICPT in SS junctions and IAR in NS junctions). MAR therefore marks the opposite, mesoscopic extreme of superconducting transport compared to the stochastic regime discussed in this chapter.

1.5 Experimental Realization

1.6 TODO

bin am überlegen die schemata maximal im Anhang zu zeigen (so probig aus dem Poster screenshoten.) Ich finde man muss viel und lange erklären was wann für vereinfachungen gelten und wie die Bilder gemeint sind. richtige physik lässt sich damit nur schwer machen. Lieber mehr IV zeigen!

- check consistency:
 - quasi-particle
 - Cooper-pair
 - aluminum
 - weak-coupling
 - normal state
 - - or -
 - bei Modell namen (Tien–Gordon, Ginzburg–Landau)
- check consistency seeblau100

theory

- table with theories

basics figures

- Landauer channels picture (mode counting + partial reflection)
- Atomic contact orbitals set channels sketch
- Microwave drive / phase-factor / photon sidebands figure
- DOS figure. parabolic and nearly constant around EF

macro

- overlapping wave functions
- rscj shalplan (mini)

- plots (a lot of them)
- do the citations

meso

- check ABS section
- PAAR
- PAMAR
- do the citations

stochastic

- alles

experiment and state of the art

- alles

References

- [1] Heike Kamerlingh Onnes and H. Kamerlingh Onnes. "Further experiments with Liquid Helium". In: *Through Measurement to Knowledge* 124c (1991). Ed. by Kostas Gavroglu and Yorgos Goudaroulis. In collab. with Robert S. Cohen. Series Title: Boston Studies in the Philosophy of Science, pp. 267–272. DOI: 10.1007/978-94-009-2079-8_17. URL: http://link.springer.com/10.1007/978-94-009-2079-8_17 (visited on 11/18/2025).
- [2] W. Meissner and R. Ochsenfeld. "Ein neuer Effekt bei Eintritt der Supraleitfähigkeit". In: *Naturwissenschaften* 21.44 (Nov. 1, 1933), pp. 787–788. ISSN: 1432-1904. DOI: 10.1007/BF01504252. URL: <https://doi.org/10.1007/BF01504252> (visited on 11/18/2025).
- [3] Neil W. Ashcroft and N. Mermin. *Solid State Physics*. South Melbourne: Cengage Learning, 2012. 848 pp. ISBN: 978-0-03-083993-1.
- [4] Rudolf Gross and Achim Marx. *Festkörperphysik*. De Gruyter Oldenbourg, Oct. 23, 2014. ISBN: 978-3-11-035870-4. DOI: 10.1524/9783110358704. URL: <https://www.degruyterbrill.com/document/doi/10.1524/9783110358704/html?lang=de> (visited on 12/17/2025).
- [5] M. Born and R. Oppenheimer. "Zur Quantentheorie der Moleküle". In: *Annalen der Physik* 389.20 (1927). _eprint: <https://onlinelibrary.wiley.com/doi/pdf/10.1002/andp.19273892002>. pp. 457–484. ISSN: 1521-3889. DOI: 10.1002/andp.19273892002. URL: <https://onlinelibrary.wiley.com/doi/abs/10.1002/andp.19273892002> (visited on 12/17/2025).
- [6] Felix Bloch. "Über die Quantenmechanik der Elektronen in Kristallgittern". In: *Zeitschrift für Physik* 52.7 (July 1, 1929), pp. 555–600. ISSN: 0044-3328. DOI: 10.1007/BF01339455. URL: <https://doi.org/10.1007/BF01339455> (visited on 12/17/2025).
- [7] Clarence Zener. "A theory of the electrical breakdown of solid dielectrics". In: *Proceedings of the Royal Society of London. Series A, Containing Papers of a Mathematical and Physical Character* 145.855 (July 2, 1934), pp. 523–529. ISSN: 0950-1207. DOI: 10.1098/rspa.1934.0116. URL: <https://doi.org/10.1098/rspa.1934.0116> (visited on 12/17/2025).
- [8] L. D. Landau. "The Theory of a Fermi Liquid". In: *Zh. Eksp. Teor. Fiz.* 30.6 (1956), p. 1058.

- [9] Georg Simon Ohm. *Die galvanische Kette, mathematisch bearbeitet*. In collab. with Bavarian State Library. Berlin : Riemann, 1827. 259 pp. URL: http://archive.org/details/bub_gb_tTVQAAAcAAJ (visited on 12/17/2025).
- [10] P. Drude. "Zur Elektronentheorie der Metalle". In: *Annalen der Physik* 306.3 (1900). _eprint: <https://onlinelibrary.wiley.com/doi/pdf/10.1002/andp.19003060312>. pp. 566–613. ISSN: 1521-3889. DOI: 10.1002/andp.19003060312. URL: <https://onlinelibrary.wiley.com/doi/abs/10.1002/andp.19003060312> (visited on 12/17/2025).
- [11] Gerd Bergmann. "Weak localization in thin films: a time-of-flight experiment with conduction electrons". In: *Physics Reports* 107.1 (May 1, 1984), pp. 1–58. ISSN: 0370-1573. DOI: 10.1016/0370-1573(84)90103-0. URL: <https://www.sciencedirect.com/science/article/pii/0370157384901030> (visited on 12/18/2025).
- [12] P. A. Lee and A. Douglas Stone. "Universal Conductance Fluctuations in Metals". In: *Physical Review Letters* 55.15 (Oct. 7, 1985). Publisher: American Physical Society, pp. 1622–1625. DOI: 10.1103/PhysRevLett.55.1622. URL: <https://link.aps.org/doi/10.1103/PhysRevLett.55.1622> (visited on 12/18/2025).
- [13] Patrick A. Lee and T. V. Ramakrishnan. "Disordered electronic systems". In: *Reviews of Modern Physics* 57.2 (Apr. 1, 1985). Publisher: American Physical Society, pp. 287–337. DOI: 10.1103/RevModPhys.57.287. URL: <https://link.aps.org/doi/10.1103/RevModPhys.57.287> (visited on 12/18/2025).
- [14] P. W. Anderson. "Absence of Diffusion in Certain Random Lattices". In: *Physical Review* 109.5 (Mar. 1, 1958). Publisher: American Physical Society, pp. 1492–1505. DOI: 10.1103/PhysRev.109.1492. URL: <https://link.aps.org/doi/10.1103/PhysRev.109.1492> (visited on 12/17/2025).
- [15] Lukas Schertel, Oliver Irtenkauf, Christof M. Aegerter, Georg Maret, and Geoffroy J. Aubry. "Magnetic-field effects on one-dimensional Anderson localization of light". In: *Physical Review A* 100.4 (Oct. 14, 2019), p. 043818. ISSN: 2469-9926, 2469-9934. DOI: 10.1103/PhysRevA.100.043818. URL: <https://link.aps.org/doi/10.1103/PhysRevA.100.043818> (visited on 03/13/2025).
- [16] Rolf Landauer. "Electrical resistance of disordered one-dimensional lattices". In: *The Philosophical Magazine: A Journal of Theoretical Experimental and Applied Physics* 21.172 (Apr. 1, 1970). Publisher: Taylor & Francis _eprint: <https://doi.org/10.1080/14786437008238472>, pp. 863–867. ISSN: 0031-8086. DOI: 10.1080/14786437008238472. URL: <https://doi.org/10.1080/14786437008238472> (visited on 12/17/2025).

- [17] M. Büttiker. "Four-Terminal Phase-Coherent Conductance". In: *Physical Review Letters* 57.14 (Oct. 6, 1986). Publisher: American Physical Society, pp. 1761–1764. DOI: 10.1103/PhysRevLett.57.1761. URL: <https://link.aps.org/doi/10.1103/PhysRevLett.57.1761> (visited on 12/17/2025).
- [18] C. W. J. Beenakker. "Random-matrix theory of quantum transport". In: *Reviews of Modern Physics* 69.3 (July 1, 1997). Publisher: American Physical Society, pp. 731–808. DOI: 10.1103/RevModPhys.69.731. URL: <https://link.aps.org/doi/10.1103/RevModPhys.69.731> (visited on 12/18/2025).
- [19] E. Scheer, P. Joyez, D. Esteve, C. Urbina, and M. H. Devoret. "Conduction Channel Transmissions of Atomic-Size Aluminum Contacts". In: *Physical Review Letters* 78.18 (May 5, 1997). Publisher: American Physical Society, pp. 3535–3538. DOI: 10.1103/PhysRevLett.78.3535. URL: <https://link.aps.org/doi/10.1103/PhysRevLett.78.3535> (visited on 03/13/2025).
- [20] Elke Scheer, Nicolás Agraít, Juan Carlos Cuevas, Alfredo Levy Yeyati, Bas Ludoph, Alvaro Martín-Rodero, Gabino Rubio Bollinger, Jan M. van Ruitenbeek, and Cristián Urbina. "The signature of chemical valence in the electrical conduction through a single-atom contact". In: *Nature* 394.6689 (July 1998). Publisher: Nature Publishing Group, pp. 154–157. ISSN: 1476-4687. DOI: 10.1038/28112. URL: <https://www.nature.com/articles/BF28112> (visited on 03/14/2025).
- [21] Nicolás Agraít, Alfredo Levy Yeyati, and Jan M. van Ruitenbeek. "Quantum Properties of Atomic-Sized Conductors". In: *ResearchGate* (Aug. 5, 2025). DOI: 10.1016/S0370-1573(02)00633-6. URL: https://www.researchgate.net/publication/1837133_Quantum_Properties_of_Atomic-Sized_Conductors (visited on 12/18/2025).
- [22] Katrin Steinberg, Marc Scheffler, and Martin Dressel. "Quasi-Particle Dynamics in Superconducting Aluminum". In: *Physical Review B* 77.21 (June 18, 2008), p. 214517. ISSN: 1098-0121, 1550-235X. DOI: 10.1103/PhysRevB.77.214517. arXiv: 0712.3391 [cond-mat]. URL: <http://arxiv.org/abs/0712.3391> (visited on 12/18/2025).
- [23] Michael Tinkham. *Introduction to Superconductivity*. 2nd ed. Mineola, NY: Dover Publications Inc., June 14, 2004. 454 pp. ISBN: 978-0-486-43503-9.
- [24] Conal E. Murray. "Material matters in superconducting qubits". In: *Materials Science and Engineering: R: Reports* 146 (Oct. 1, 2021), p. 100646. ISSN: 0927-796X. DOI: 10.1016/j.mser.2021.100646. URL: <https://www.sciencedirect.com/science/article/pii/S0927796X21000413> (visited on 12/18/2025).

- [25] M. T. A. Saif, S. Zhang, A. Haque, and K. J. Hsia. "Effect of native Al₂O₃ on the elastic response of nanoscale Al films". In: *Acta Materialia* 50.11 (June 28, 2002), pp. 2779–2786. ISSN: 1359-6454. DOI: 10.1016/S1359-6454(02)00089-7. URL: <https://www.sciencedirect.com/science/article/pii/S1359645402000897> (visited on 12/18/2025).
- [26] B. D. Josephson. "Possible new effects in superconductive tunnelling". In: *Physics Letters* 1.7 (July 1, 1962), pp. 251–253. ISSN: 0031-9163. DOI: 10.1016/0031-9163(62)91369-0. URL: <https://www.sciencedirect.com/science/article/pii/0031916362913690> (visited on 12/18/2025).
- [27] Sidney Shapiro. "Josephson Currents in Superconducting Tunneling: The Effect of Microwaves and Other Observations". In: *Physical Review Letters* 11.2 (July 15, 1963). Publisher: American Physical Society, pp. 80–82. DOI: 10.1103/PhysRevLett.11.80. URL: <https://link.aps.org/doi/10.1103/PhysRevLett.11.80> (visited on 03/16/2025).
- [28] P. K. Tien and J. P. Gordon. "Multiphoton Process Observed in the Interaction of Microwave Fields with the Tunneling between Superconductor Films". In: *Physical Review* 129.2 (Jan. 15, 1963). Publisher: American Physical Society, pp. 647–651. DOI: 10.1103/PhysRev.129.647. URL: <https://link.aps.org/doi/10.1103/PhysRev.129.647> (visited on 03/13/2025).
- [29] N. R. Werthamer, E. Helfand, and P. C. Hohenberg. "Temperature and Purity Dependence of the Superconducting Critical Field, $\$H_{c2}\$$. III. Electron Spin and Spin-Orbit Effects". In: *Physical Review* 147.1 (July 8, 1966). Publisher: American Physical Society, pp. 295–302. DOI: 10.1103/PhysRev.147.295. URL: <https://link.aps.org/doi/10.1103/PhysRev.147.295> (visited on 12/18/2025).
- [30] Leon N. Cooper. "Bound Electron Pairs in a Degenerate Fermi Gas". In: *Physical Review* 104.4 (Nov. 15, 1956). Publisher: American Physical Society, pp. 1189–1190. DOI: 10.1103/PhysRev.104.1189. URL: <https://link.aps.org/doi/10.1103/PhysRev.104.1189> (visited on 11/18/2025).
- [31] J. Bardeen, L. N. Cooper, and J. R. Schrieffer. "Microscopic Theory of Superconductivity". In: *Physical Review* 106.1 (Apr. 1, 1957). Publisher: American Physical Society, pp. 162–164. DOI: 10.1103/PhysRev.106.162. URL: <https://link.aps.org/doi/10.1103/PhysRev.106.162> (visited on 10/31/2025).
- [32] Bernhard Mühlischlegel. "Die thermodynamischen Funktionen des Supraleiters". In: *Zeitschrift für Physik* 155.3 (June 1, 1959), pp. 313–327. ISSN: 0044-3328. DOI: 10.1007/BF01332932. URL: <https://doi.org/10.1007/BF01332932> (visited on 11/18/2025).

- [33] R. C. Dynes, V. Narayanamurti, and J. P. Gorno. "Direct Measurement of Quasiparticle-Lifetime Broadening in a Strong-Coupled Superconductor". In: *Physical Review Letters* 41.21 (Nov. 20, 1978). Publisher: American Physical Society, pp. 1509–1512. DOI: 10.1103/PhysRevLett.41.1509. URL: <https://link.aps.org/doi/10.1103/PhysRevLett.41.1509> (visited on 10/30/2025).
- [34] J. Bardeen. "Tunnelling from a Many-Particle Point of View". In: *Physical Review Letters* 6.2 (Jan. 15, 1961). Publisher: American Physical Society, pp. 57–59. DOI: 10.1103/PhysRevLett.6.57. URL: <https://link.aps.org/doi/10.1103/PhysRevLett.6.57> (visited on 11/18/2025).
- [35] Ivar Giaever. "Electron Tunneling Between Two Superconductors". In: *Physical Review Letters* 5.10 (Nov. 15, 1960), pp. 464–466. ISSN: 0031-9007. DOI: 10.1103/PhysRevLett.5.464. URL: <https://link.aps.org/doi/10.1103/PhysRevLett.5.464> (visited on 11/18/2025).
- [36] Ivar Giaever and Karl Megerle. "Study of Superconductors by Electron Tunneling". In: *Physical Review* 122.4 (May 15, 1961). Publisher: American Physical Society, pp. 1101–1111. DOI: 10.1103/PhysRev.122.1101. URL: <https://link.aps.org/doi/10.1103/PhysRev.122.1101> (visited on 11/18/2025).